Applied Superconductivity:

Josephson Effect and Superconducting Electronics

Manuscript to the Lectures during WS 2003/2004, WS 2005/2006, WS 2006/2007, WS 2007/2008, WS 2008/2009, and WS 2009/2010

Prof. Dr. Rudolf Gross

and

Dr. Achim Marx

Walther-Meißner-Institut

Bayerische Akademie der Wissenschaften

and

Lehrstuhl für Technische Physik (E23)

Technische Universität München

Walther-Meißner-Strasse 8

D-85748 Garching

Rudolf.Gross@wmi.badw.de

Contents

Preface **xxi**

I Foundations of the Josephson Effect **1**

1 Macroscopic Quantum Phenomena **3**

1.1 The Macroscopic Quantum Model 3

1.1.1 Coherent Phenomena in Superconductivity 3

1.1.2 Macroscopic Quantum Currents in Superconductors 12

1.1.3 The London Equations 18

1.2 Flux Quantization 24

1.2.1 Flux and Fluxoid Quantization 26

1.2.2 Experimental Proof of Flux Quantization 28

1.2.3 Additional Topic: Rotating Superconductor 30

1.3 Josephson Effect 32

1.3.1 The Josephson Equations 33

1.3.2 Josephson Tunneling 37

2 JJs: The Zero Voltage State **43**

2.1 Basic Properties of Lumped Josephson Junctions 44

2.1.1 The Lumped Josephson Junction 44

2.1.2 The Josephson Coupling Energy 45

2.1.3 The Superconducting State 47

2.1.4 The Josephson Inductance 49

2.1.5 Mechanical Analogs 49

2.2 Short Josephson Junctions 50

2.2.1 Quantum Interference Effects – Short Josephson Junction in an Applied Magnetic Field 50

2.2.2 The Fraunhofer Diffraction Pattern 54
2.2.3 Determination of the Maximum Josephson Current Density 58
2.2.4 Additional Topic: Direct Imaging of the Supercurrent Distribution 62
2.2.5 Additional Topic: Short Josephson Junctions: Energy Considerations 63
2.2.6 The Motion of Josephson Vortices 65
2.3 Long Josephson Junctions 68
2.3.1 The Stationary Sine-Gordon Equation 68
2.3.2 The Josephson Vortex 70
2.3.3 Junction Types and Boundary Conditions 73
2.3.4 Additional Topic: Josephson Current Density Distribution and Maximum Josephson Current 79
2.3.5 The Pendulum Analog 84

3 JJs: The Voltage State 89

3.1 The Basic Equation of the Lumped Josephson Junction 90
3.1.1 The Normal Current: Junction Resistance 90
3.1.2 The Displacement Current: Junction Capacitance 92
3.1.3 Characteristic Times and Frequencies 93
3.1.4 The Fluctuation Current 94
3.1.5 The Basic Junction Equation 96
3.2 The Resistively and Capacitively Shunted Junction Model 97
3.2.1 Underdamped and Overdamped Josephson Junctions 100
3.3 Response to Driving Sources 102
3.3.1 Response to a dc Current Source 102
3.3.2 Response to a dc Voltage Source 107
3.3.3 Response to ac Driving Sources 107
3.3.4 Photon-Assisted Tunneling 112
3.4 Additional Topic: Effect of Thermal Fluctuations 115
3.4.1 Underdamped Junctions: Reduction of I_c by Premature Switching 117
3.4.2 Overdamped Junctions: The Ambegaokar-Halperin Theory 118
3.5 Secondary Quantum Macroscopic Effects 122
3.5.1 Quantum Consequences of the Small Junction Capacitance 122

3.5.2 Limiting Cases: The Phase and Charge Regime . . . 125
3.5.3 Coulomb and Flux Blockade . . . 128
3.5.4 Coherent Charge and Phase States . . . 130
3.5.5 Quantum Fluctuations . . . 132
3.5.6 Macroscopic Quantum Tunneling . . . 133
3.6 Voltage State of Extended Josephson Junctions . . . 139
3.6.1 Negligible Screening Effects . . . 139
3.6.2 The Time Dependent Sine-Gordon Equation . . . 140
3.6.3 Solutions of the Time Dependent Sine-Gordon Equation . . . 141
3.6.4 Additional Topic: Resonance Phenomena . . . 144

II Applications of the Josephson Effect 153

4 SQUIDs 157
4.1 The dc-SQUID . . . 159
4.1.1 The Zero Voltage State . . . 159
4.1.2 The Voltage State . . . 164
4.1.3 Operation and Performance of dc-SQUIDs . . . 168
4.1.4 Practical dc-SQUIDs . . . 172
4.1.5 Read-Out Schemes . . . 176
4.2 Additional Topic: The rf-SQUID . . . 180
4.2.1 The Zero Voltage State . . . 180
4.2.2 Operation and Performance of rf-SQUIDs . . . 182
4.2.3 Practical rf-SQUIDs . . . 186
4.3 Additional Topic: Other SQUID Configurations . . . 188
4.3.1 The DROS . . . 188
4.3.2 The SQIF . . . 189
4.3.3 Cartwheel SQUID . . . 189
4.4 Instruments Based on SQUIDs . . . 191
4.4.1 Magnetometers . . . 192
4.4.2 Gradiometers . . . 194
4.4.3 Susceptometers . . . 196

4.4.4 Voltmeters . . . 197
4.4.5 Radiofrequency Amplifiers . . . 198
4.5 Applications of SQUIDs . . . 200
4.5.1 Biomagnetism . . . 200
4.5.2 Nondestructive Evaluation . . . 204
4.5.3 SQUID Microscopy . . . 206
4.5.4 Gravity Wave Antennas and Gravity Gradiometers . . . 208
4.5.5 Geophysics . . . 210

5 Digital Electronics 215
5.1 Superconductivity and Digital Electronics . . . 216
5.1.1 Historical development . . . 217
5.1.2 Advantages and Disadvantages of Josephson Switching Devices . . . 219
5.2 Voltage State Josephson Logic . . . 222
5.2.1 Operation Principle and Switching Times . . . 222
5.2.2 Power Dissipation . . . 225
5.2.3 Switching Dynamics, Global Clock and Punchthrough . . . 226
5.2.4 Josephson Logic Gates . . . 228
5.2.5 Memory Cells . . . 234
5.2.6 Microprocessors . . . 236
5.2.7 Problems of Josephson Logic Gates . . . 237
5.3 RSFQ Logic . . . 239
5.3.1 Basic Components of RSFQ Circuits . . . 241
5.3.2 Information in RSFQ Circuits . . . 246
5.3.3 Basic Logic Gates . . . 247
5.3.4 Timing and Power Supply . . . 249
5.3.5 Maximum Speed . . . 249
5.3.6 Power Dissipation . . . 250
5.3.7 Prospects of RSFQ . . . 250
5.3.8 Fabrication Technology . . . 253
5.3.9 RSFQ Roadmap . . . 254
5.4 Analog-to-Digital Converters . . . 255
5.4.1 Additional Topic: Foundations of ADCs . . . 256
5.4.2 The Comparator . . . 261
5.4.3 The Aperture Time . . . 263
5.4.4 Different Types of ADCs . . . 264

6 The Josephson Voltage Standard 269

6.1 Voltage Standards . . . 270

6.1.1 Standard Cells and Electrical Standards . . . 270

6.1.2 Quantum Standards for Electrical Units . . . 271

6.2 The Josephson Voltage Standard . . . 274

6.2.1 Underlying Physics . . . 274

6.2.2 Development of the Josephson Voltage Standard . . . 274

6.2.3 Junction and Circuit Parameters for Series Arrays . . . 279

6.3 Programmable Josephson Voltage Standard . . . 281

6.3.1 Pulse Driven Josephson Arrays . . . 283

7 Superconducting Photon and Particle Detectors 285

7.1 Superconducting Microwave Detectors: Heterodyne Receivers . . . 286

7.1.1 Noise Equivalent Power and Noise Temperature . . . 286

7.1.2 Operation Principle of Mixers . . . 287

7.1.3 Noise Temperature of Heterodyne Receivers . . . 290

7.1.4 SIS Quasiparticle Mixers . . . 292

7.1.5 Josephson Mixers . . . 296

7.2 Superconducting Microwave Detectors: Direct Detectors . . . 297

7.2.1 NEP of Direct Detectors . . . 298

7.3 Thermal Detectors . . . 300

7.3.1 Principle of Thermal Detection . . . 300

7.3.2 Bolometers . . . 302

7.3.3 Antenna-Coupled Microbolometers . . . 307

7.4 Superconducting Particle and Single Photon Detectors . . . 314

7.4.1 Thermal Photon and Particle Detectors: Microcalorimeters . . . 314

7.4.2 Superconducting Tunnel Junction Photon and Particle Detectors . . . 318

7.5 Other Detectors . . . 328

8 Microwave Applications 329

8.1 High Frequency Properties of Superconductors . . . 330

8.1.1 The Two-Fluid Model . . . 330

8.1.2 The Surface Impedance . . . 333

8.2 Superconducting Resonators and Filters . . . 336

8.3 Superconducting Microwave Sources . . . 337

9 Superconducting Quantum Bits **339**

9.1 Quantum Bits and Quantum Computers . . . 341

9.1.1 Quantum Bits . . . 341

9.1.2 Quantum Computing . . . 343

9.1.3 Quantum Error Correction . . . 346

9.1.4 What are the Problems? . . . 348

9.2 Implementation of Quantum Bits . . . 349

9.3 Why Superconducting Qubits . . . 352

9.3.1 Superconducting Island with Leads . . . 352

III Anhang **355**

A The Josephson Equations **357**

B Imaging of the Maximum Josephson Current Density **361**

C Numerical Iteration Method for the Calculation of the Josephson Current Distribution **363**

D Photon Noise **365**

I Power of Blackbody Radiation . . . 365

II Noise Equivalent Power . . . 367

E Qubits **369**

I What is a quantum bit ? . . . 369

I.1 Single-Qubit Systems . . . 369

I.2 The spin-1/2 system . . . 371

I.3 Two-Qubit Systems . . . 372

II Entanglement . . . 373

III Qubit Operations . . . 375

III.1 Unitarity . . . 375

III.2 Single Qubit Operations . . . 375

III.3 Two Qubit Operations . . . 376

IV Quantum Logic Gates . . . 377

IV.1 Single-Bit Gates . . . 377

IV.2 Two Bit Gates . . . 379

V The No-Cloning Theorem . . . 384

VI Quantum Complexity . . . 385

VII The Density Matrix Representation . . . 385

F Two-Level Systems **389**

I Introduction to the Problem . . . 389

I.1 Relation to Spin-1/2 Systems . . . 390

II Static Properties of Two-Level Systems . . . 390

II.1 Eigenstates and Eigenvalues . . . 390

II.2 Interpretation . . . 391

II.3 Quantum Resonance . . . 394

III Dynamic Properties of Two-Level Systems . . . 395

III.1 Time Evolution of the State Vector . . . 395

III.2 The Rabi Formula . . . 395

G The Spin 1/2 System **399**

I Experimental Demonstration of Angular Momentum Quantization . . . 399

II Theoretical Description . . . 401

II.1 The Spin Space . . . 401

III Evolution of a Spin 1/2 Particle in a Homogeneous Magnetic Field . . . 402

IV Spin 1/2 Particle in a Rotating Magnetic Field . . . 404

IV.1 Classical Treatment . . . 404

IV.2 Quantum Mechanical Treatment . . . 406

IV.3 Rabi's Formula . . . 407

H Literature **409**

I Foundations of Superconductivity . . . 409

I.1 Introduction to Superconductivity . . . 409

I.2 Early Work on Superconductivity and Superfluidity . . . 410

I.3 History of Superconductivity . . . 410

I.4 Weak Superconductivity, Josephson Effect, Flux Structures . . . 410

II Applications of Superconductivity . . . 411

II.1 Electronics, Sensors, Microwave Devices . . . 411

II.2 Power Applications, Magnets, Transportation . . . 412

II.3 Superconducting Materials . . . 412

I SI-Einheiten **413**

I Geschichte des SI Systems . . . 413

II Die SI Basiseinheiten . . . 415

III Einige von den SI Einheiten abgeleitete Einheiten . . . 416

IV Vorsätze . . . 418

V Abgeleitete Einheiten und Umrechnungsfaktoren . . . 419

J Physikalische Konstanten **425**

List of Figures

1.1 Meissner-Effect . . . 19
1.2 Current transport and decay of a supercurrent in the Fermi sphere picture . . . 20
1.3 Stationary Quantum States . . . 24
1.4 Flux Quantization in Superconductors . . . 25
1.5 Flux Quantization in a Superconducting Cylinder . . . 27
1.6 Experiment by Doll and Naebauer . . . 29
1.7 Experimental Proof of Flux Quantization . . . 29
1.8 Rotating superconducting cylinder . . . 31
1.9 The Josephson Effect in weakly coupled superconductors . . . 32
1.10 Variation of $n_s^\star$ and γ across a Josephson junction . . . 35
1.11 Schematic View of a Josephson Junction . . . 36
1.12 Josephson Tunneling . . . 39

2.1 Lumped Josephson Junction . . . 45
2.2 Coupling Energy and Josephson Current . . . 46
2.3 The Tilted Washboard Potential . . . 48
2.4 Extended Josephson Junction . . . 51
2.5 Magnetic Field Dependence of the Maximum Josephson Current . . . 55
2.6 Josephson Current Distribution in a Small Josephson Junction for Various Applied Magnetic Fields . . . 56
2.7 Spatial Interference of Macroscopic Wave Funktions . . . 57
2.8 The Josephson Vortex . . . 57
2.9 Gaussian Shaped Josephson Junction . . . 59
2.10 Comparison between Measurement of Maximum Josephson Current and Optical Diffraction Experiment . . . 60
2.11 Supercurrent Auto-correlation Function . . . 61
2.12 Magnetic Field Dependence of the Maximum Josephson Current of a YBCO-GBJ . . . 63

2.13 Motion of Josephson Vortices 66
2.14 Magnetic Flux and Current Density Distribution for a Josephson Vortex 70
2.15 Classification of Junction Types: Overlap, Inline and Grain Boundary Junction 74
2.16 Geometry of the Asymmetric Inline Junction 77
2.17 Geometry of Mixed Overlap and Inline Junctions 78
2.18 The Josephson Current Distribution of a Long Inline Junction 80
2.19 The Maximum Josephson Current as a Function of the Junction Length 81
2.20 Magnetic Field Dependence of the Maximum Josephson Current and the Josephson Current Density Distribution in an Overlap Junction 83
2.21 The Maximum Josephson Current as a Function of the Applied Field for Overlap and Inline Junctions 84

3.1 Current-Voltage Characteristic of a Josephson tunnel junction 91
3.2 Equivalent circuit for a Josephson junction including the normal, displacement and fluctuation current 92
3.3 Equivalent circuit of the Resistively Shunted Junction Model 97
3.4 The Motion of a Particle in the Tilt Washboard Potential 98
3.5 Pendulum analogue of a Josephson junction 99
3.6 The IVCs for Underdamped and Overdamped Josephson Junctions 101
3.7 The time variation of the junction voltage and the Josephson current 103
3.8 The RSJ model current-voltage characteristics 105
3.9 The RCSJ Model IVC at Intermediate Damping 107
3.10 The RCJ Model Circuit for an Applied dc and ac Voltage Source 108
3.11 Overdamped Josephson Junction driven by a dc and ac Voltage Source 110
3.12 Overdamped Josephson junction driven by a dc and ac Current Source 111
3.13 Shapiro steps for under- and overdamped Josephson junction 112
3.14 Photon assisted tunneling 113
3.15 Photon assisted tunneling in SIS Josephson junction 113
3.16 Thermally Activated Phase Slippage 116
3.17 Temperature Dependence of the Thermally Activated Junction Resistance 119
3.18 RSJ Model Current-Voltage Characteristics Including Thermally Activated Phase Slippage 120
3.19 Variation of the Josephson Coupling Energy and the Charging Energy with the Junction Area 124
3.20 Energy diagrams of an isolated Josephson junction 127
3.21 The Coulomb Blockade 128

3.22 The Phase Blockade . . . 129
3.23 The Cooper pair box . . . 131
3.24 Double well potential for the generation of phase superposition states . . . 132
3.25 Macroscopic Quantum Tunneling . . . 134
3.26 Macroscopic Quantum Tunneling at Large Damping . . . 138
3.27 Mechanical analogue for phase dynamics of a long Josephson junction . . . 141
3.28 The Current Voltage Characteristic of an Underdamped Long Josephson Junction . . . 145
3.29 Zero field steps in IVCs of an annular Josephson junction . . . 147

4.1 The dc-SQUID . . . 160
4.2 Maximum Supercurrent versus Applied Magnetic Flux for a dc-SQUID at Weak Screening 162
4.3 Total Flux versus Applied Magnetic Flux for a dc SQUID at $\beta_L > 1$ . . . 163
4.4 Current-voltage Characteristics of a dc-SQUID at Negligible Screening . . . 165
4.5 The pendulum analogue of a dc SQUID . . . 167
4.6 Principle of Operation of a dc-SQUID . . . 169
4.7 Energy Resolution of dc-SQUIDs . . . 172
4.8 The Practical dc-SQUID . . . 173
4.9 Geometries for thin film SQUID washers . . . 174
4.10 Flux focusing effect in a $YBa_2Cu_3O_{7-\delta}$ washer . . . 175
4.11 The Washer dc-SQUID . . . 176
4.12 The Flux Modulation Scheme for a dc-SQUID . . . 177
4.13 The Modulation and Feedback Circuit of a dc-SQUID . . . 178
4.14 The rf-SQUID . . . 180
4.15 Total flux versus applied flux for a rf-SQUID . . . 182
4.16 Operation of rf-SQUIDs . . . 183
4.17 Tank voltage versus rf-current for a rf-SQUID . . . 184
4.18 High T_c rf-SQUID . . . 187
4.19 The double relaxation oscillation SQUID (DROS) . . . 188
4.20 The Superconducting Quantum Interference Filter (SQIF) . . . 190
4.21 Input Antenna for SQUIDs . . . 191
4.22 Various types of thin film SQUID magnetometers . . . 193
4.23 Magnetic noise signals . . . 194
4.24 Magnetically shielded room . . . 195
4.25 Various gradiometers configurations . . . 196

4.26 Miniature SQUID Susceptometer . . . 197
4.27 SQUID Radio-frequency Amplifier . . . 198
4.28 Multichannel SQUID Systems . . . 201
4.29 Magnetocardiography . . . 203
4.30 Magnetic field distribution during R peak . . . 204
4.31 SQUID based nondestructive evaluation . . . 205
4.32 Scanning SQUID microscopy . . . 207
4.33 Scanning SQUID microscopy images . . . 208
4.34 Gravity wave antenna . . . 209
4.35 Gravity gradiometer . . . 210

5.1 Cryotron . . . 217
5.2 Josephson Cryotron . . . 218
5.3 Device performance of Josephson devices . . . 220
5.4 Principle of operation of a Josephson switching device . . . 222
5.5 Output current of a Josephson switching device . . . 224
5.6 Threshold characteristics for a magnetically and directly coupled gate . . . 229
5.7 Three-junction interferometer gate . . . 230
5.8 Current injection device . . . 230
5.9 Josephson Atto Weber Switch (JAWS) . . . 231
5.10 Direct coupled logic (DCL) gate . . . 231
5.11 Resistor coupled logic (RCL) gate . . . 232
5.12 4 junction logic (4JL) gate . . . 232
5.13 Non-destructive readout memory cell . . . 234
5.14 Destructive read-out memory cell . . . 235
5.15 4 bit Josephson microprocessor . . . 237
5.16 Josephson microprocessor . . . 238
5.17 Comparison of latching and non-latching Josephson logic . . . 240
5.18 Generation of SFQ Pulses . . . 242
5.19 dc to SFQ Converter . . . 243
5.20 Basic Elements of RSFQ Circuits . . . 244
5.21 RSFQ memory cell . . . 245
5.22 RSFQ logic . . . 246
5.23 RSFQ OR and AND Gate . . . 247

5.24 RSFQ NOT Gate . . . 248
5.25 RSFQ Shift Register . . . 249
5.26 RSFQ Microprocessor . . . 253
5.27 RSFQ roadmap . . . 254
5.28 Principle of operation of an analog-to-digital converter . . . 256
5.29 Analog-to-Digital Conversion . . . 257
5.30 Semiconductor and Superconductor Comparators . . . 262
5.31 Incremental Quantizer . . . 263
5.32 Flash-type ADC . . . 265
5.33 Counting-type ADC . . . 266

6.1 Weston cell . . . 271
6.2 The metrological triangle for the electrical units . . . 273
6.3 IVC of an underdamped Josephson junction under microwave irradiation . . . 275
6.4 International voltage comparison between 1920 and 2000 . . . 276
6.5 One-Volt Josephson junction array . . . 277
6.6 Josephson series array embedded into microwave stripline . . . 278
6.7 Microwave design of Josephson voltage standards . . . 279
6.8 Adjustment of Shapiro steps for a series array Josephson voltage standard . . . 281
6.9 IVC of overdamped Josephson junction with microwave irradiation . . . 282
6.10 Programmable Josephson voltage standard . . . 283

7.1 Block diagram of a heterodyne receiver . . . 288
7.2 Ideal mixer as a switch . . . 288
7.3 Current response of a heterodyne mixer . . . 289
7.4 IVCs and IF output power of SIS mixer . . . 290
7.5 Optimum noise temperature of a SIS quasiparticle mixer . . . 293
7.6 Measured DSB noise temperature of a SIS quasiparticle mixers . . . 294
7.7 High frequency coupling schemes for SIS mixers . . . 295
7.8 Principle of thermal detectors . . . 301
7.9 Operation principle of superconducting transition edge bolometer . . . 302
7.10 Sketch of a HTS bolometer . . . 305
7.11 Specific detectivity of various bolometers . . . 305
7.12 Relaxation processes in a superconductor after energy absorption . . . 307
7.13 Antenna-coupled microbolometer . . . 308

7.14 Schematic illustration of the hot electron bolometer mixer . . . 309
7.15 Hot electron bolometer mixers with different antenna structures . . . 311
7.16 Transition-edge sensors . . . 315
7.17 Transition-edge sensors . . . 317
7.18 Functional principle of a superconducting tunnel junction detector . . . 319
7.19 Circuit diagram of a superconducting tunnel junction detector . . . 319
7.20 Energy resolving power of STJDs . . . 321
7.21 Quasiparticle tunneling in SIS junctions . . . 323
7.22 Quasiparticle trapping in STJDs . . . 326
7.23 STJDs employing lateral quasiparticle trapping . . . 326
7.24 Superconducting tunnel junction x-ray detector . . . 327

8.1 Equivalent circuit for the two-fluid model . . . 332
8.2 Characteristic frequency regimes for a superconductor . . . 332
8.3 Surface resistance of Nb and Cu . . . 335

9.1 Konrad Zuse 1945 . . . 341
9.2 Representation of a Qubit State as a Vector on the Bloch Sphere . . . 342
9.3 Operational Scheme of a Quantum Computer . . . 344
9.4 Quantum Computing: What's it good for? . . . 345
9.5 Shor, Feynman, Bennett and Deutsch . . . 346
9.6 Qubit Realization by Quantum Mechanical Two level System . . . 349
9.7 Use of Superconductors for Qubits . . . 352
9.8 Superconducting Island with Leads . . . 354

E.1 The Bloch Sphere S^2 . . . 370
E.2 The Spin-1/2 System . . . 371
E.3 Entanglement – an artist's view. . . . 373
E.4 Classical Single-Bit Gate . . . 377
E.5 Quantum NOT Gate . . . 378
E.6 Classical Two Bit Gate . . . 380
E.7 Reversible and Irreversible Logic . . . 380
E.8 Reversible Classical Logic . . . 381
E.9 Reversible XOR (CNOT) and SWAP Gate . . . 382
E.10 The Controlled U Gate . . . 382

E.11 Density Matrix for Pure Single Qubit States 386
E.12 Density Matrix for a Coherent Superposition of Single Qubit States 387

F.1 Energy Levels of a Two-Level System 392
F.2 The Benzene Molecule 394
F.3 Graphical Representation of the Rabi Formula 396

G.1 The Larmor Precession 400
G.2 The Rotating Reference Frame 404
G.3 The Effective Magnetic Field in the Rotating Reference Frame 405
G.4 Rabi's Formula for a Spin 1/2 System 408

List of Tables

5.1 Switching delay and power dissipation for various types of logic gates. 233

5.2 Josephson 4 kbit RAM characteristics (organization: 4096 word x 1 bit, NEC). 236

5.3 Performance of various logic gates 237

5.4 Possible applications of superconductor digital circuits (source: SCENET 2001). 251

5.5 Performance of various RSFQ based circuits. 252

7.1 Characteristic materials properties of some superconductors 325

8.1 Important high-frequency characteristic of superconducting and normal conducting . . . 334

E.1 Successive measurements on a two-qubit state showing the results A and B with the corresponding probabilities $P(A)$ and $P(B)$ and the remaining state after the measurement. . . . 373

Chapter 2

Physics of Josephson Junctions: The Zero Voltage State

In this chapter we discuss the physics of Josephson junctions in the zero voltage state. In this situation the Josephson current density J_s always is smaller than the maximum Josephson current density J_c so that the current is flowing as supercurrent that can be described by the macroscopic quantum approach. The voltage state of Josephson junctions will be discussed in chapter 3. In the case of a finite junction voltage the situation is more complex, since besides the Josephson current other types of current such as a normal current or a displacement current have to be taken into account. These currents vanish in the zero voltage state and hence make the treatment of this situation simple.

In section 2.1 we first restrict ourselves to cases where the junction area is small enough so that the junction can be considered as a zero-dimensional or lumped element. Then the integral current rather than the current density is sufficient to describe the Josephson junction properties. We will introduce the ***Josephson coupling energy*** and the ***Josephson inductance*** as well as mechanical analogs for lumped Josephson junctions.

In sections 2.2 and 2.3 we then relax the restriction on the junction area and discuss the junctions as distributed systems, where the currents have a spatial dependence inside the junction itself. Here, the discussion of the magnetic field dependence of the Josephson current density is the main topic.

2.1 Basic Properties of Lumped Josephson Junctions

In many superconducting devices and circuits Josephson junctions with very small spatial dimensions are used. Such small Josephson junctions can be understood by considering the gauge invariant phase difference and the current density to be uniform over the junction area. We will show later (see sections 2.2 and 2.3) that small means that the spatial extension of the junction area must be much smaller than a characteristic screening length, the so-called ***Josephson penetration depth*** λ_J. This screening length of a weak superconducting system is the analog of the ***London penetration depth*** λ_L of a bulk superconductor and sets the length scale over which variations of the supercurrent density occur. Therefore, the supercurrent density across a Josephson junction can be assumed to be constant, if the junction area is much smaller than this screening length. In the same way the supercurrent density in a bulk superconductor always can be assumed constant, if the spatial dimensions of the bulk superconductor are much smaller the London penetration depth.

We recall that the London penetration depth $\lambda_L = \sqrt{m^\star/\mu_0 n_s^\star q^{\star 2}}$ defines the length scale over which an applied field can penetrate a bulk superconductor. Equivalently, it defines the surface layer, in which the screening currents are flowing. This length scale typically ranges between several 10 nm and about 1 μm for most superconductors. For a weak superconducting system as a Josephson junction the equivalent screening length is much larger. This can be understood simply by the fact that in the weak region connecting two bulk superconductors the density of Cooper pairs is strongly reduced. Since the screening length is proportional to $1/\sqrt{n_s^\star}$, the corresponding screening length λ_J is strongly increased. It easily can be larger than 100 μm. That is, even Josephson junctions with spatial dimensions of the order of several 10 μm can be considered small.

2.1.1 The Lumped Josephson Junction

We call Josephson junctions with spatially homogeneous supercurrent density and phase difference ***lumped junctions***. Such junctions can be described by a supercurrent

$$I_s = \int_S \mathbf{J}_s \cdot d\mathbf{s} \ . \tag{2.1.1}$$

The region of integration is the junction area S. The current-phase relation (1.3.7) can be rewritten in terms of the currents as

$$I_s(t) = I_c \sin\varphi(t) \ . \tag{2.1.2}$$

The gauge-invariant phase difference is still given by

$$\varphi(t) = \theta_2(t) - \theta_1(t) - \frac{2\pi}{\Phi_0} \int_1^2 \mathbf{A}(\mathbf{r},t) \cdot d\mathbf{l} \ . \tag{2.1.3}$$

The voltage-phase relation $\frac{\partial\varphi}{\partial t} = \frac{2\pi}{\Phi_0} \int_1^2 \mathbf{E}(\mathbf{r},t) \cdot d\mathbf{l}$ can be simplified by noting that $\int_1^2 \mathbf{E}(\mathbf{r},t) \cdot d\mathbf{l}$ is just the voltage $V(t)$ across the junction. Note that the voltage is constant across the junction area extending for example in the yz-plane, since for a lumped junction the electric field is independent of y and z. The voltage-phase relation then becomes

$$\frac{d\varphi}{dt} = \frac{2\pi}{\Phi_0} V \ . \tag{2.1.4}$$

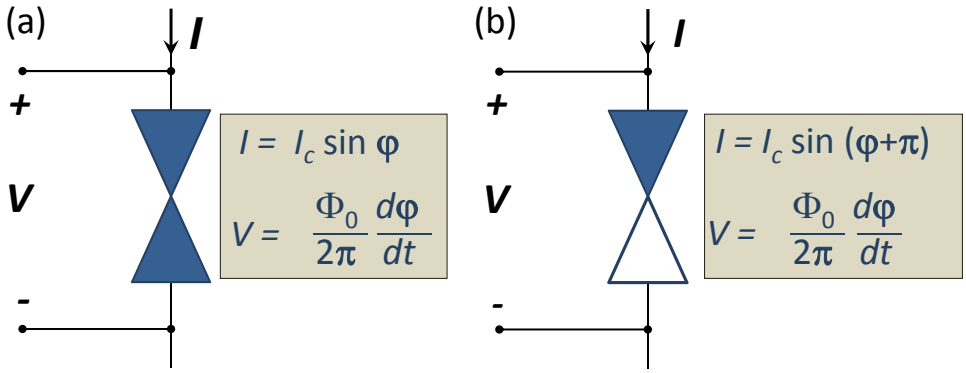

Figure 2.1: The Josephson junction as a lumped circuit element, which is characterized by the crossed symbol in circuit diagrams and is governed by the two Josephson equations. Left: "0"-junction, right: "π"-junction.

Note that we are now using the total derivative because for a lumped junction the phase difference φ does not depend on any spatial coordinate.

Fig. 2.1 shows the symbol for a lumped Josephson junction along with the two equations describing the junction. As we discuss later, we have to distinguish between "0"-junctions, for which $I_s = I_c \sin(0+\varphi) = I_c \sin\varphi$, and so-called "$\pi$"-junctions, for which $I_s = I_c \sin(\pi+\varphi) = -I_c \sin\varphi$. That is, for the same phase difference φ the Josephson current I_s is flowing in opposite directions for "0"- and "π"-junctions. In the following subsections we discuss how energy can be stored in a lumped junction and how it behaves when it is driven by external current or voltage sources.

2.1.2 The Josephson Coupling Energy

Due to the zero junction voltage, no energy will be dissipated in the junction residing in the superconducting (S) state. However, there is a finite energy stored in the junction. This energy can be considered as a molecular binding energy caused by the finite overlap of the macroscopic wavefunctions of the two weakly coupled superconductors. The magnitude of the binding energy becomes immediately evident by considering the process of increasing the junction current from zero to a finite value I. Let the initial value of the phase difference φ be zero at zero junction current. As we are increasing the current, according to the current-phase relation also the phase difference φ has to change. Furthermore, according to the voltage-phase relation a changing phase difference corresponds to a finite junction voltage. That is, on increasing the current the external source has to supply energy that is determined by the integral of the power $I \cdot V$ during the current increase. Although the superelectrons can flow across the junction without causing any resistance, on increasing the current we have to accelerate the superelectrons in the sample and this requires a certain amount of energy. This energy is then stored by the moving superelectrons. The described process can be viewed as a conversion of potential into kinetic energy. Upon reaching the critical current I_c, the whole potential ("binding") energy is converted into kinetic energy.

In order to calculate the energy stored in the Josephson junction we have to integrate the power from time $t = 0$ when we start the current increase to time $t = t_0$ when we are stopping the increase:

$$E_J = \int_0^{t_0} I_s V \, dt \ . \tag{2.1.5}$$

Here, V is the voltage applied during increasing the current from zero at $t = 0$ to the final value I at time

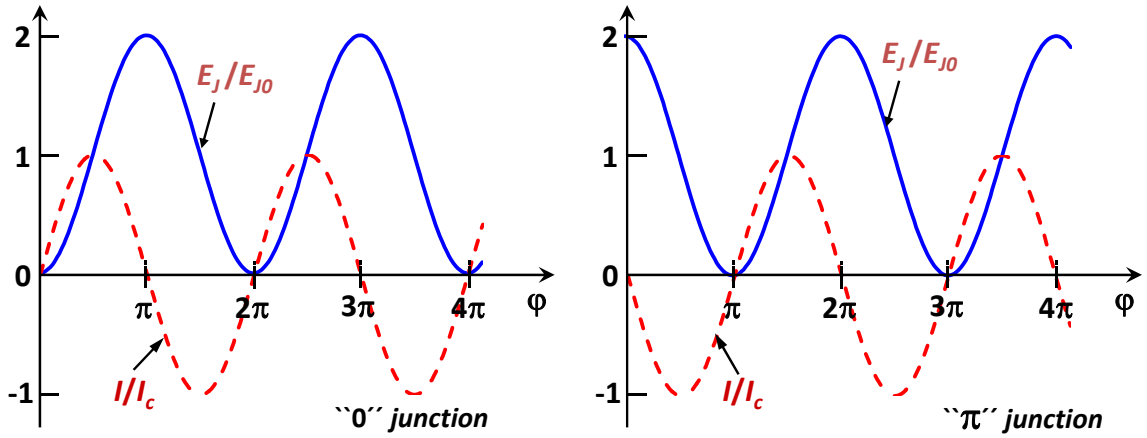

Figure 2.2: The normalized Josephson current I_s/I_c and the normalized coupling energy E_J/E_{J0} plotted versus the phase difference φ. Left: "0"-junction, right: "π"-junction

t_0. Using the current-phase and the voltage-phase relation we obtain

$$E_J = \int_0^{t_0} (I_c \sin\widetilde{\varphi}) \left(\frac{\Phi_0}{2\pi}\frac{d\widetilde{\varphi}}{dt}\right) dt \ . \tag{2.1.6}$$

With the phase difference $\varphi(0) = 0$ and $\varphi(t_0) = \varphi$ we can write the integral as

$$E_J = \frac{\Phi_0 I_c}{2\pi} \int_0^{\varphi} \sin\widetilde{\varphi}\, d\widetilde{\varphi} \ . \tag{2.1.7}$$

Integration gives the energy stored in the junction as

$$\boxed{E_J = \frac{\Phi_0 I_c}{2\pi}(1-\cos\varphi) = E_{J0}(1-\cos\varphi)} \ . \tag{2.1.8}$$

This energy is usually denoted as the ***Josephson coupling energy***. Similar to the binding energy of a molecule this energy results from the overlap (or coupling) of the wave functions of the two superconducting electrodes.

In Fig. 2.2 we have plotted the coupling energy and the Josephson current as a function of the phase difference. The energy is lowest, if no current flows and φ is zero or a multiple of 2π. Therefore, such junctions are denoted as "0" junctions. There are also other junctions (e.g. junctions with ferromagnetic barrier layers) for which the state of lowest coupling energy is obtained for a phase difference of π or $(2n+1)\pi$. These junctions are named "π" junctions.

We briefly discuss the order of magnitude of the Josephson coupling energy. For a junction with a typical critical current of 1 mA we have $E_{J0} \simeq 3\times10^{-19}$J what corresponds to the thermal energy k_BT of around 20 000 K. Therefore, thermal smearing effects are negligible. However, for junctions with very small critical current this is different. For example, for $I_c = 1\,\mu$A the coupling energy corresponds to the thermal energy at around 20 K and, hence, thermal smearing effects become prominent as discussed in chapter 3.

2.1.3 The Superconducting State

According to the current-phase relation (2.1.2) a constant dc current imposed on a Josephson junction by an external current source results in a constant phase difference

$$\varphi = \varphi_n = \arcsin\left(\frac{I}{I_c}\right) + 2\pi n \tag{2.1.9}$$

$$\varphi = \widetilde{\varphi}_n = \pi - \arcsin\left(\frac{I}{I_c}\right) + 2\pi n \tag{2.1.10}$$

for

$$-I_c \leq I \leq +I_c \ . \tag{2.1.11}$$

The constant phase difference results in $d\varphi/dt = 0$. Hence, each of the solutions corresponds to zero junction voltage and describes the superconducting state. We will call this situation the ***zero voltage state*** or stationary (S) state.

In order to analyze the stability of the zero voltage state we use the potential energy $E_{\rm pot}$ of the system Josephson junction + current source. To find $E_{\rm pot}$ we use the rule, which is general for any subsystem (the Josephson junction in our case) under the action of a constant external force F (the applied current in our case), saying that the total energy G is equal to the difference of the two terms:[1]

$$G = E - F \cdot x \ . \tag{2.1.12}$$

Here, E is the intrinsic (free) energy of the subsystem and x is its generalized coordinate corresponding to the generalized force $F = I$. The coordinate should be chosen in a way that the product $F\dot{x}$ gives the power P flowing into the subsystem. Since for the Josephson junction the latter product equals to $I \cdot V$, the desirable coordinate is

$$x = \int V\, dt = \frac{\hbar}{2e}\varphi + c = \frac{\Phi_0}{2\pi}\varphi + c \ , \tag{2.1.13}$$

where c is an integration constant. The potential energy of the system is thus given by

$$E_{\rm pot}(\varphi) = E_J(\varphi) - I\left(\frac{\Phi_0}{2\pi}\varphi + c\right) = E_{J0}\left[1 - \cos\varphi - \frac{I}{I_c}\varphi\right] + \widetilde{c} \ . \tag{2.1.14}$$

As shown by Fig. 2.3, the function $E_{\rm pot}(\varphi)$ has the shape of a tilted washboard and is therefore often called the ***tilted washboard potential***. The washboard has minima and maxima for the values of the phase difference given by (2.1.9) and (2.1.10), respectively. It is evident that the former solutions are stable and the latter are unstable. We further note that the states corresponding to different n are physically equivalent and therefore we usually only refer to the $n = 0$ solution.

[1] Note that in thermodynamics G is called the Gibbs energy (potential) of the subsystem, which has to be distinguished from the free energy (Helmholtz energy) E.

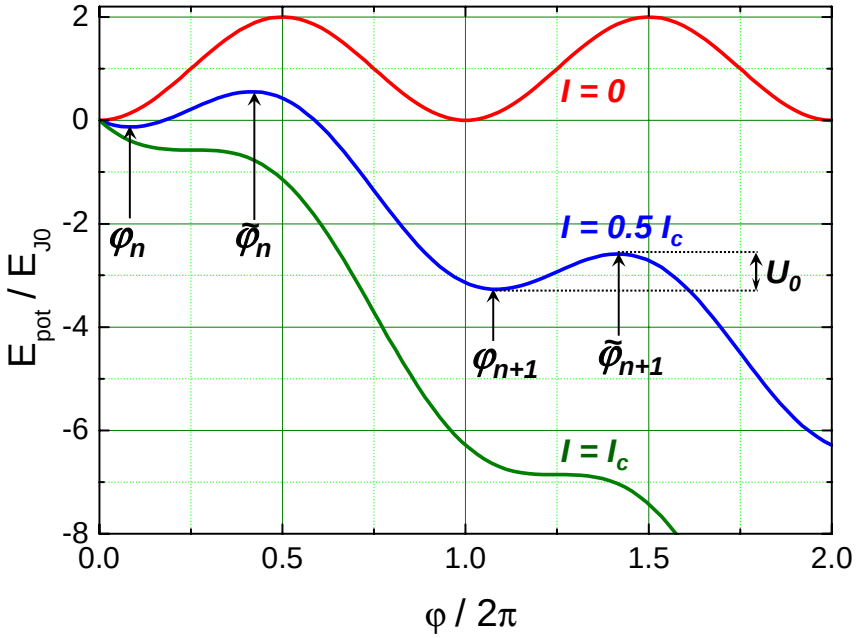

Figure 2.3: The potential energy $E_{\rm pot}(\varphi)$ of a current biased lumped Josephson junction at various values of the applied current. The potential is named tilted washboard potential.

By analyzing the tilted washboard potential, from (2.1.14) we can easily derive the difference $U_0 = E_{\rm pot}(\varphi_n) - E_{\rm pot}(\widetilde{\varphi}_n)$ and the curvature $k \equiv \partial^2 E_{\rm pot}/\partial\varphi^2$ of the potential at the potential minimum. We obtain[2]

$$U_0 \equiv E_{\rm pot}(\varphi_n) - E_{\rm pot}(\widetilde{\varphi}_n) = 2E_{J0}\left[\sqrt{1-\left(\frac{I}{I_c}\right)^2} - \frac{I}{I_c}\arccos\left(\frac{I}{I_c}\right)\right] \tag{2.1.15}$$

$$k \equiv \frac{\partial^2 E_{\rm pot}}{\partial\varphi^2} = E_{J0}\sqrt{1-\left(\frac{I}{I_c}\right)^2}\ . \tag{2.1.16}$$

We see that these quantities approach zero for $I \to I_c$. Close to the critical current we have $\alpha \equiv 1 - I/I_c \ll 1$ and can use the following approximations

$$\varphi_0 = \frac{\pi}{2} - \sqrt{2\alpha}\,, \qquad \widetilde{\varphi}_0 = \frac{\pi}{2} + \sqrt{2\alpha} \tag{2.1.17}$$

$$U_0 = \frac{2}{3}E_{J0}\,(2\alpha)^{2/3} \tag{2.1.18}$$

$$k = E_{J0}\,(2\alpha)^{1/2}\ . \tag{2.1.19}$$

We will see in chapter 3 that the tilted washboard potential is very useful for describing the dynamics of Josephson junctions at $I > I_c$. It is evident from (2.1.14) and Fig. 2.3 that in this case there are no longer any minima in the potential and consequently the phase will continuously increase resulting in a finite junction voltage. The dynamics can be described by considering the phase as a particle moving down the tilted washboard potential. However, in order to describe this process we have to determine the mass of the particle and the damping of the motion. This can be done only after introducing the other current components as the normal current and the displacement current in chapter 3.

[2]Here we use the equality $\arcsin(x) = (\pi/2) - \arccos(x) = \arccos\sqrt{1-x^2}$.

2.1.4 The Josephson Inductance

Energy storage and conservation in the Josephson junction suggests that it can be considered as a ***nonlinear reactance***. In order to clarify this we consider the time derivative of the current-phase relation

$$\frac{dI_s}{dt} = I_c \cos\varphi \frac{d\varphi}{dt} . \tag{2.1.20}$$

Using the voltage-phase relation we obtain

$$\frac{dI_s}{dt} = I_c \cos\varphi \frac{2\pi}{\Phi_0} V . \tag{2.1.21}$$

This immediately shows that for small variations of the current around the value $I_s = I_c \sin\varphi$ the Josephson junctions behaves as an inductance

$$L_s = \frac{\Phi_0}{2\pi I_c \cos\varphi} = L_c \frac{1}{\cos\varphi} \qquad \text{with} \qquad L_c = \frac{\hbar}{2eI_c} . \tag{2.1.22}$$

A very unusual property of this ***Josephson inductance*** is the fact that it can have negative values in the intervals $\pi/2 + 2\pi n < \varphi < 3\pi/2 + 2\pi n$. Note that from the electrotechnical point of view the energy E_J can be considered as stored in the inductance L_s. The fact that the Josephson inductance can have negative values results in a behavior that is completely different from an ordinary nonlinear inductance. This is immediately seen, if we apply a constant voltage V to the Josephson junction. In this case we obtain an oscillating Josephson current as discussed already in section 1.3.1. Note that for an ordinary inductance the current would not oscillate but just gradually increase. The oscillations of the supercurrent are called ***Josephson oscillations*** and have been predicted in the original paper by Brian Josephson. These oscillations accompany most processes in Josephson junctions and are of particular importance for their dynamics as we will see in chapter 3.

2.1.5 Mechanical Analogs

The unusual properties of the supercurrent has stimulated the search for mechanical analogs that can be used to better understand the dynamics of the Josephson junction. The first example is a plane mechanical pendulum in a uniform gravity field. Here, the phase difference φ plays the role of the angle of the pendulum with respect to its equilibrium position. The supercurrent corresponds to the torque and the voltage to the angular velocity of the pendulum.

A second useful analog is a particle moving along the coordinate φ with velocity $v \propto d\varphi/dt \propto V$ in a potential given by (2.1.14).

2.2 Short Josephson Junctions

So far we only have considered zero-dimensional Josephson junctions with a spatially homogeneous supercurrent density. We could describe these lumped elements by the integral Josephson current I_s with its maximum value I_c and the gauge-invariant phase difference φ. In this section we relax the condition of spatially homogeneous values of the Josephson current density and the gauge-invariant phase difference and allow now for spatial variations $J_s(\mathbf{r})$ and $\varphi(\mathbf{r})$ of these quantities. We refer to such junctions as ***extended Josephson junctions***.

Discussing the physics of extended Josephson junctions we have to distinguish between two cases:

- ***Short Josephson junctions:***

  For short junctions the magnetic field generated by the Josephson current itself (self-field) is negligible compared to the externally applied magnetic field. We will show below that junctions can be considered as short junctions, if the spatial dimensions of the junction area are smaller than a characteristic length scale named ***Josephson penetration depth*** λ_J.

- ***Long Josephson junctions:***

  For long Josephson junctions the magnetic field generated by the Josephson current itself is no longer negligible. Long Josephson junctions have spatial dimensions larger than the ***Josephson penetration depth*** λ_J.

2.2.1 Quantum Interference Effects – Short Josephson Junction in an Applied Magnetic Field

The description of superconductors by a macroscopic wave function manifests itself in a number of interference effects. We already have seen in section 1.3 that the oscillation of the Josephson current in the presence of a finite potential difference between the junction electrodes can be viewed as a ***temporal interference*** between the macroscopic wave functions of the two superconducting electrodes. In the following we show that we also can observe ***spatial interference*** in Josephson junctions, if we generate spatial changes of the gauge invariant phase difference by applying an external magnetic field. We will see that the observed interference effect is completely analogous to the diffraction at a slit in optics.

We consider the cross section of an extended Josephson junction as sketched in Fig. 2.4. The two junction electrodes are separated by a thin insulating barrier of thickness d. The junction area $L \cdot W$ extends in the yz-plane and the current is flowing in the x-direction. We assume $W, L \gg d$ so that effects of the edges of the junction can be neglected. Each superconducting electrode is assumed to have thickness t_1 and t_2 larger than the London penetration depth λ_{L1} and λ_{L2} of the electrode material, respectively. An external magnetic field is applied parallel to the y-direction, that is, $\mathbf{B}_e = (0, B_y, 0)$. Since the applied field penetrates the superconducting electrode up to a thickness given by the London penetration depth, we can define a magnetic thickness of the junction given by $t_B = d + \lambda_{L1} + \lambda_{L2}$.

In order to discuss the effect of the applied magnetic field on the Josephson current density J_s we have to determine the phase shift introduced between two positions P and Q along the z-axis separated by an infinitesimal distance dz. The shift $\varphi(Q) - \varphi(P)$ of the gauge-invariant phase difference between the two points can be determined by considering the line integral along the contour shown in Fig. 2.4. We have to demand that the total phase change along the closed contour is $2\pi n$, that is

$$\begin{aligned} \oint_C \nabla\theta \cdot d\mathbf{l} &= 2\pi\, n \\ &= (\theta_{Q_b} - \theta_{Q_a}) + (\theta_{P_c} - \theta_{Q_b}) + (\theta_{P_d} - \theta_{P_c}) + (\theta_{Q_a} - \theta_{P_d}) + 2\pi\, n \end{aligned} \tag{2.2.1}$$

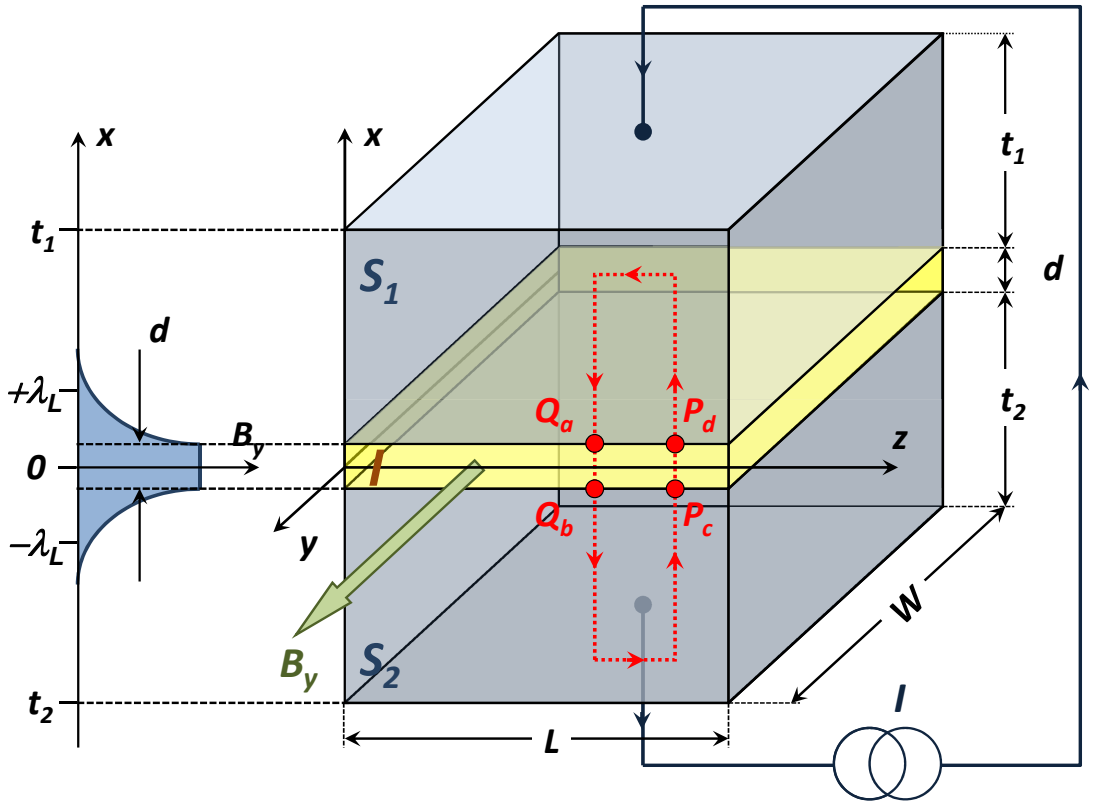

Figure 2.4: Cross section of an extended Josephson junction. The current flows in x- direction, the magnetic field is applied in y-direction. The broken line indicates the closed contour of integration. On the left hand side the decay of the magnetic field in the junction electrodes over the length scale λ_L is indicated.

For the determination of the various terms we use the expressions for the gauge invariant phase gradient in the bulk superconductors (compare (1.1.65))

$$\nabla\theta \;=\; \frac{2\pi}{\Phi_0}\left(\Lambda\mathbf{J}_s+\mathbf{A}\right) \tag{2.2.2}$$

and the gauge-invariant phase difference across the barrier (compare (1.3.2))

$$\varphi \;=\; \theta_2-\theta_1-\frac{2\pi}{\Phi_0}\int_1^2\mathbf{A}\cdot d\mathbf{l}\;. \tag{2.2.3}$$

The first and third term in (2.2.1) are the differences across the Josephson junction barrier and directly follow from (2.2.3):

$$\theta_{Q_b}-\theta_{Q_a} \;=\; +\varphi(Q)+\frac{2\pi}{\Phi_0}\int_{Q_a}^{Q_b}\mathbf{A}\cdot d\mathbf{l} \tag{2.2.4}$$

$$\theta_{P_d}-\theta_{P_c} \;=\; -\varphi(P)+\frac{2\pi}{\Phi_0}\int_{P_c}^{P_d}\mathbf{A}\cdot d\mathbf{l}\;. \tag{2.2.5}$$

The second and fourth term are differences in the superconducting material and are found from the supercurrent equation (2.2.2) for $\nabla\theta$:

$$\theta_{P_c} - \theta_{Q_b} = \int_{Q_b}^{P_c} \nabla\theta \cdot d\mathbf{l} = +\frac{2\pi}{\Phi_0}\int_{Q_b}^{P_c} \Lambda\mathbf{J}_s \cdot d\mathbf{l} + \frac{2\pi}{\Phi_0}\int_{Q_b}^{P_c} \mathbf{A} \cdot d\mathbf{l} \tag{2.2.6}$$

$$\theta_{Q_a} - \theta_{P_d} = \int_{P_d}^{Q_a} \nabla\theta \cdot d\mathbf{l} = +\frac{2\pi}{\Phi_0}\int_{P_d}^{Q_a} \Lambda\mathbf{J}_s \cdot d\mathbf{l} + \frac{2\pi}{\Phi_0}\int_{P_d}^{Q_a} \mathbf{A} \cdot d\mathbf{l} \ . \tag{2.2.7}$$

Substituting (2.2.4) – (2.2.7) into (2.2.3) yields

$$\varphi(Q) - \varphi(P) = -\frac{2\pi}{\Phi_0}\oint_C \mathbf{A} \cdot d\mathbf{l} - \frac{2\pi}{\Phi_0}\int_{Q_b}^{P_c} \Lambda\mathbf{J}_s \cdot d\mathbf{l} - \frac{2\pi}{\Phi_0}\int_{P_d}^{Q_a} \Lambda\mathbf{J}_s \cdot d\mathbf{l} \ . \tag{2.2.8}$$

The integration of $\mathbf{A}$ is around a close contour and therefore is equal to the total flux Φ inside the area enclosed by the contour. The integration of $\mathbf{J}_s$ follows the same contour C but excludes the integration over the insulating barrier. We rewrite this integral as an integral along the incomplete contour C':

$$\oint_{C'} \Lambda\mathbf{J}_s \cdot d\mathbf{l} = \int_{Q_b}^{P_c} \Lambda\mathbf{J}_s \cdot d\mathbf{l} + \int_{P_d}^{Q_a} \Lambda\mathbf{J}_s \cdot d\mathbf{l} \ . \tag{2.2.9}$$

Then, the difference of the gauge-invariant phase difference between point Q and P is obtained to

$$\varphi(Q) - \varphi(P) = -\frac{2\pi\Phi}{\Phi_0} - \frac{2\pi}{\Phi_0}\oint_{C'} \Lambda\mathbf{J}_s \cdot d\mathbf{l} \ . \tag{2.2.10}$$

Discussing the magnitude of the line integral of the current density we can note the following: First, the integration of the current density along one segment of the path in x-direction cancels with the contribution of the adjacent path, which is only an infinitesimal distance dz away. Second, each part of the integration in the z-direction is taken deep inside ($\gg \lambda_L$) the superconducting electrode, where the current density induced by the applied field is exponentially small. Furthermore, the applied current is in the negative x-direction. That is, it is perpendicular to the integration path along z and therefore contributes nothing to the integral of the current density. Therefore, the line integral of the current density vanishes and we obtain

$$\varphi(P) - \varphi(Q) = \frac{2\pi\Phi}{\Phi_0} \ . \tag{2.2.11}$$

We see that the normalized shift $[\varphi(P) - \varphi(Q)]/2\pi$ of the gauge invariant phase difference is just given by the normalized magnetic flux Φ/Φ_0 threading the junction between the positions z and $z + dz$.

Since the magnetic field decays exponentially into each superconducting electrodes the total flux enclosed by the contour line is

$$\Phi = B_y(d + \lambda_{L1} + \lambda_{L2})\, dz = B_y t_B dz \ . \tag{2.2.12}$$

Then, with $\varphi(P)-\varphi(Q)=\frac{2\pi}{\Phi_0}B_y t_B dz=\frac{\partial\varphi}{\partial z}dz$ we obtain

$$\frac{\partial\varphi}{\partial z} = \frac{2\pi}{\Phi_0}B_y t_B \tag{2.2.13}$$

We can use a similar argument by choosing point Q and P at an infinitesimal distance dy in the y-direction and obtain

$$\frac{\partial\varphi}{\partial y} = -\frac{2\pi}{\Phi_0}B_z t_B \ . \tag{2.2.14}$$

In general, we can write

$$\boxed{\nabla\varphi(\mathbf{r},t) = \frac{2\pi}{\Phi_0}t_B\ [\mathbf{B}(\mathbf{r},t)\times\widehat{\mathbf{x}}]\ ,} \tag{2.2.15}$$

where $\widehat{\mathbf{x}}$ is the unit vector in x-direction, that is the unit vector perpendicular to the junction area (anti-parallel to the current flow in our case).

Integration of (2.2.13) gives

$$\varphi(z) = \frac{2\pi}{\Phi_0}B_y t_B z+\varphi_0\ , \tag{2.2.16}$$

where the integration constant φ_0 is the phase difference at $z=0$. Using the current-phase relation we obtain the supercurrent density to

$$\boxed{J_s(y,z,t) = J_c(y,z)\ \sin\left(\frac{2\pi}{\Phi_0}t_B B_y z+\varphi_0\right) = J_c(y,z)\ \sin\left(kz+\varphi_0\right)} \tag{2.2.17}$$

with $k=\frac{2\pi}{\Phi_0}t_B B_y$. We see that J_s varies sinusoidally along the z-direction with the oscillation period $\Delta z=2\pi/k$ given by $\Phi_0/t_B B_y$. That is, Δz is inversely proportional to the product of the applied field and the effective magnetic thickness. We also immediately see that $\Delta z t_B B_y=\Phi=\Phi_0$, i.e. the magnetic flux through the junction within a single oscillation period corresponds to a single flux quantum.

So far we have assumed that the thickness of the junction electrodes is much larger than the London penetration depth. If $t_1<\lambda_{L1}$ and $t_2<\lambda_{L2}$ the magnetic field penetrates the complete electrode and the Meißner shielding currents are less than those in thick electrodes. As a result the effective value of the magnetic thickness of the junction increases and the magnetic thickness t_B has to be replaced by

$$\widetilde{t_B} = d+\lambda_{L1}\coth\frac{t_1}{\lambda_{L1}}+\lambda_{L2}\coth\frac{t_2}{\lambda_{L2}}\ . \tag{2.2.18}$$

2.2.2 The Fraunhofer Diffraction Pattern

In this subsection we discuss, how the integral current $I_s = \iint J_s(y,z)dydz$ across the junction depends on the applied magnetic field. We first integrate the maximum Josephson current density $J_c(y,z)$ in the direction of the applied magnetic field. If the external field is in y-direction ($\mathbf{B}_e = (0, B_y, 0)$) we obtain

$$i_c(z) = \int_{-W/2}^{W/2} J_c(y,z)\, dy \ . \tag{2.2.19}$$

With this expression, according to (2.2.17) we obtain

$$I_s(B_y) = \int_{-L/2}^{L/2} i_c(z)\, \sin(kz + \varphi_0)\, dz \ . \tag{2.2.20}$$

This expression is equivalent to

$$I_s(B_y) = \Im \left\{ e^{\imath\varphi_0} \int_{-\infty}^{\infty} i_c(z)\, e^{\imath kz}\, dz \right\} \ , \tag{2.2.21}$$

where $k = \frac{2\pi}{\Phi_0} t_B B_y$. Since $i_c(z)$ is zero outside the junction, i.e. for $|z| > L/2$, we have replaced the integration limits by $\pm\infty$.

In general, the integral in (2.2.21) is a complex number with magnitude and phase. When the integral is multiplied by $e^{\imath\varphi_0}$, only the phase but not the magnitude changes. Therefore, the maximum Josephson current I_s^m is just given by the magnitude of the integral, that is by

$$I_s^m(B_y) = \left| \int_{-\infty}^{\infty} i_c(z)\, e^{\imath kz}\, dz \right| \ . \tag{2.2.22}$$

This integral represents a Fourier integral, that is, the magnetic field dependence of the maximum Josephson current I_s^m is given by the Fourier transform of the function $i_c(z)$. This is completely analogous to optics, where the intensity of the light behind a slit of width L and transmission function $i_c(z)$ is given by the Fourier transform of the transmission function.

If the maximum Josephson current density $J_c(y,z)$ of the junction is spatially homogeneous, the magnitude of $i_c(z)$ is constant for $-L/2 \le z \le +L/2$ and zero for $|z| > L/2$. In this case the $I_s^m(B_y)$ dependence is equivalent to the diffraction pattern of a slit of width L with constant transmission i_c. The diffraction pattern is the well known ***Fraunhofer diffraction pattern*** shown by Fig. 2.5:

$$I_s^m(\Phi) = I_c \left| \frac{\sin\frac{kL}{2}}{\frac{kL}{2}} \right| = I_c \left| \frac{\sin\frac{\pi\Phi}{\Phi_0}}{\frac{\pi\Phi}{\Phi_0}} \right| \ . \tag{2.2.23}$$

Here, $\Phi = B_y t_b L$ is the flux through the junction and $I_c = i_c L$. We note that the experimental observation of the Fraunhofer diffraction pattern $I_s^m(\Phi)$ given by (2.2.23) was very important to prove the Josephson

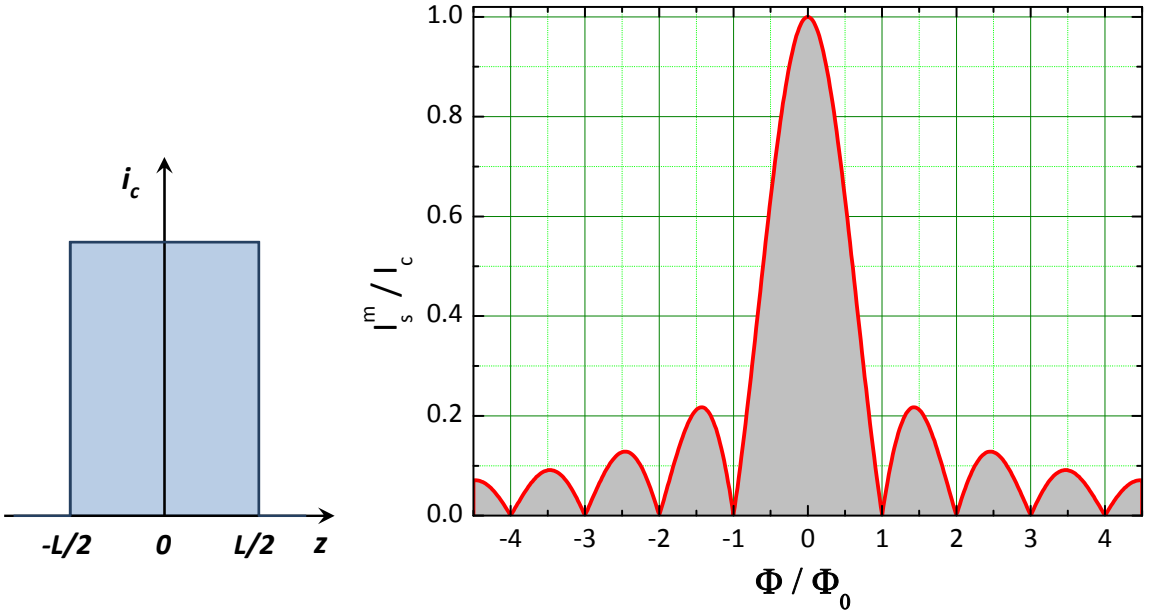

Figure 2.5: Magnetic field dependence of the maximum Josephson current I_s^m of a short Josephson junction. On the left the maximum current density integrated along the magnetic field direction, $i_c(z) = \int J_c(y,z)dy$, is shown for the case of a spatially homogeneous maximum current density $J_c(y,z)$.

tunneling of Cooper pairs. From the experimental point of view it was unclear whether the measured supercurrent in a superconductor/insulator/superconductor tunnel junction is flowing as a homogeneous Josephson tunneling current or just through small pinholes in the tunneling barrier. However, if the latter would have been true, no Fraunhofer diffraction pattern would have been observed for the $I_s^m(\Phi)$ dependence.

To understand the shape of the $I_s^m(\Phi)$ dependence we consider the spatial distribution of $i_s(z) = \int J_s(y,z)dy$ along the z-direction for a magnetic field applied in y-direction. For zero field, that is $\Phi = 0$ the gauge-invariant phase difference is constant, $\varphi(z) = \varphi_0$, and hence $i_s(z) = const$. The maximum Josephson current is obtained for $\varphi_0 = -\pi/2$, that is, $J_s(y,z) = -J_c(y,z)$ (note that the current is flowing in negative x-direction, see Fig. 2.6a). If we feed a current less than the maximum Josephson current through the junction, we have $\varphi_0 \neq \pi/2$ and the local current density is just $J_s(y,z) = J_c(y,z)\sin\varphi_0 < J_c(y,z)$.

We next consider the case of an externally applied magnetic flux of $\Phi = \Phi_0/2$. In this case according to (2.2.16) the gauge-invariant phase difference $\varphi(z)$ varies as

$$\varphi(z) \;=\; \frac{2\pi\Phi}{\Phi_0}\,\frac{z}{L} + \varphi_0 \;=\; \frac{\pi z}{L} + \varphi_0 \;. \tag{2.2.24}$$

Therefore, the supercurrent density varies sinusoidally with z. The difference of the phases between the two edges of the junction is

$$\varphi(L/2) - \varphi(-L/2) \;=\; \pi \;. \tag{2.2.25}$$

That means that half of a full oscillation period fits into the junction. This situation is shown in Fig. 2.6b. Which half period to put into the junction depends on the choice of φ_0. In Fig. 2.6b we have made the choice $\varphi_0 = -\pi/2$. In this case the phase difference increases from $-\pi$ at $z = -L/2$ to 0 at $z = +L/2$. This choice gives the maximum possible Josephson current I_c^m in negative x-direction. Note that for $\varphi = 0$ we obtain a vanishing total Josephson current.

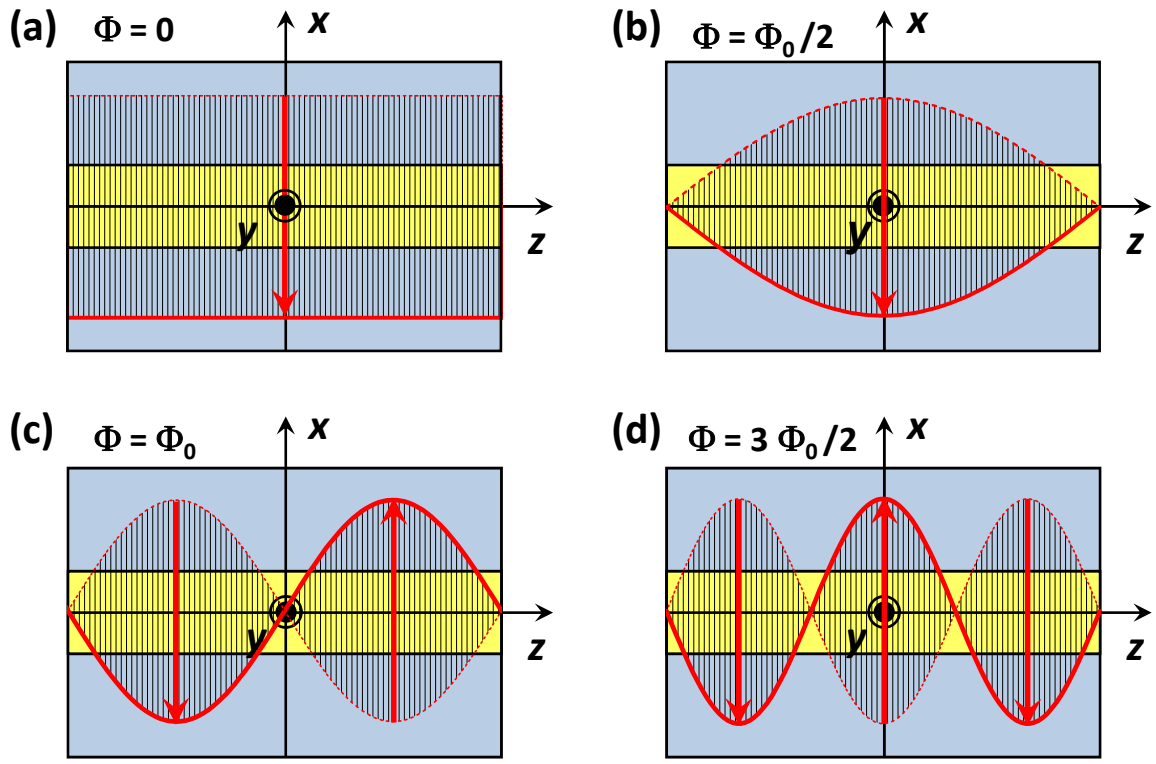

Figure 2.6: The Josephson current density distribution along a small Josephson junction extending from $-L/2$ to $+L/2$ in z-direction. (a) $\Phi = 0$, $\varphi_0 = -\pi/2$ (b) $\Phi = \frac{1}{2}\Phi_0$, $\varphi_0 = -\pi/2$, (c) $\Phi = \Phi_0$, $\varphi_0 = 0$ and (d) $\Phi = \frac{3}{2}\Phi_0$, $\varphi_0 = +\pi/2$. The magnetic field is applied in y-direction. The external current is applied in negative x-direction.

In Fig. 2.6c and d we show the situation for $\Phi = \Phi_0$ and $\Phi = \frac{3}{2}\Phi_0$, respectively. For $\Phi = \Phi_0$ the total phase difference from one edge of the junction to the other is 2π and a complete oscillation period of the Josephson current density fits into the junction. In this case the total Josephson current is zero irrespective of the choice of φ_0. For $\Phi = \frac{3}{2}\Phi_0$ the total phase difference from one edge to the other is 3π and one and a half oscillation periods of the Josephson current density fit into the junction. The current from the full period is zero and the total current is determined by a half period. Of course, the total current is smaller than for $\Phi = \Phi_0/2$ when a half period fits the whole junction. This shows that the Josephson current generally tends to decrease with increasing applied magnetic field as shown in Fig. 2.5.

In order to illustrate the magnetic field dependence of the maximum Josephson current as the result of a spatial interference effect of the macroscopic wave functions in the two superconducting electrodes we consider Fig. 2.7. Superconductor 1 is described by a plane wave with the plane of constant phase parallel to the barrier. In the same way, superconductors 2 is described by a plane wave, however, with the plane of constant phase tilted due to the phase shift caused by the magnetic field B_y. The phase shift at position z is given by $\delta\varphi(z) = \frac{2\pi}{\Phi_0} B_y t_B z + \varphi_0$. For the situation shown in Fig. 2.7 we immediately see that each partial wave has a counterpart with a phase shift of π causing destructive interference. This is just the situation where the total Josephson current through the junction is zero.

We discuss in more detail the situation for $\Phi = \Phi_0$ shown in Fig. 2.6c. Evidently in this situation the Josephson current density flows in negative and positive x-direction on the left and right side of the junction, respectively. The question is, how the supercurrent density can have such pattern across the insulating barrier without any net driving current. The solution is shown in Fig. 2.8. The supercurrent on the left side turns around in the bottom electrode so as to match the supercurrent density in the insulator on the right side. Actually the supercurrent has to bend to avoid the penetration of the applied magnetic field into the electrode material over a length scale larger than the London penetration depth.

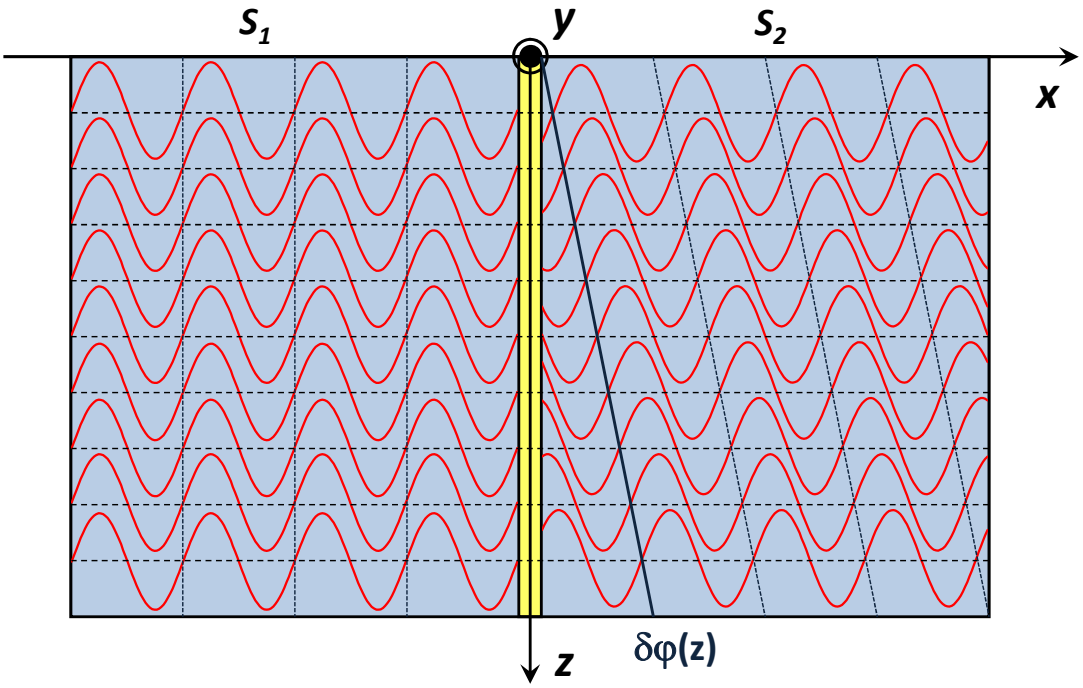

Figure 2.7: Illustration of the magnetic field dependence of the maximum Josephson current as a spatial quantum interference phenomenon. The applied magnetic field B_y causes a position dependent phase shift $\delta\varphi(z) = \frac{2\pi}{\Phi_0} B_y t_B z + \varphi_0$ (we have chosen $\varphi_0 = 0$ for simplicity).

The resulting supercurrent density pattern resembles the pattern of an Abrikosov vortex in a type-II superconductor and is known as ***Josephson vortex***. Note that in contrast to an Abrikosov vortex the Josephson vortex does not need to have a normal core. The vortex core is located in the barrier region where the pair density is exponentially small.

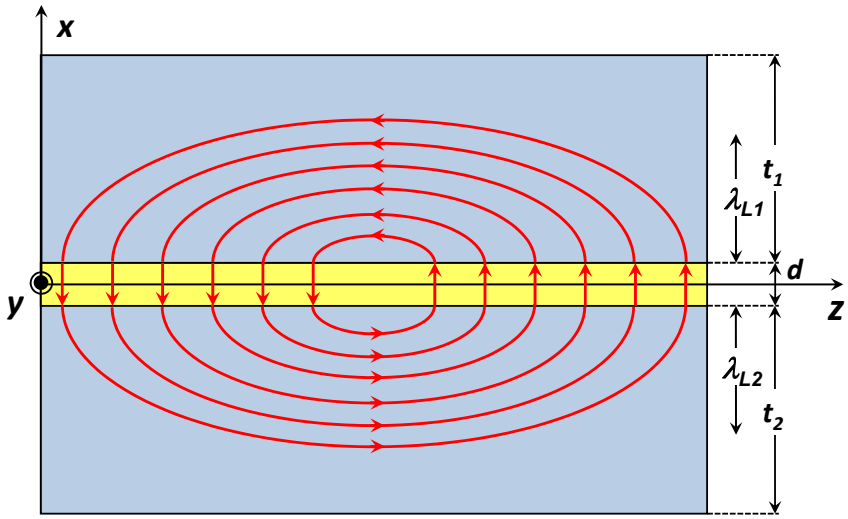

Figure 2.8: The supercurrent distribution in the superconducting electrodes and across the insulator for the case $\Phi = \Phi_0$. The pattern in known as the Josephson vortex.

Arbitrary Magnetic Field Direction

We consider a short Josephson junction as shown in Fig. 2.4 and let the applied magnetic field lie in an arbitrary direction within the plane of the junction barrier so that

$$\mathbf{B}_e = B_y\,\hat{\mathbf{y}} + B_z\,\hat{\mathbf{z}}\ . \tag{2.2.26}$$

Here, $\hat{\mathbf{y}}$ and $\hat{\mathbf{z}}$ are the unit vectors in y- and z-direction. By generalizing the arguments given above, for this situation the magnetic field dependence of the maximum Josephson current can be expressed as

$$I_s^m(\Phi) = I_c \left| \frac{\sin\frac{\pi\Phi_y}{\Phi_0}}{\frac{\pi\Phi_y}{\Phi_0}} \right| \left| \frac{\sin\frac{\pi\Phi_z}{\Phi_0}}{\frac{\pi\Phi_z}{\Phi_0}} \right| , \tag{2.2.27}$$

where $\Phi_y = B_y t_b L$ and $\Phi_z = B_z t_b W$. Equivalently, we can write

$$I_s^m(\mathbf{B}_e) = \left| \int_S J_c(y,z)\, \mathrm{e}^{i\mathbf{k}\cdot\mathbf{r}}\, dS \right| . \tag{2.2.28}$$

Here, $S = L \cdot W$ is the junction area, $\mathbf{r}$ the position vector in the two-dimensional yz-plane, and dS the differential area element in that plane.

2.2.3 Determination of the Maximum Josephson Current Density

In real Josephson junctions usually the critical current density $J_c(y,z)$ is spatially inhomogeneous due imperfections of the fabrication process or a spatially varying thickness of the tunneling barrier. That is, this quantity usually is not known. Therefore, for researchers fabricating Josephson junctions it would be very desirable to be able to determine the spatial distribution $J_c(y,z)$ experimentally. A suitable method would be the measurement of the $I_s^m(\Phi)$ dependence. However, it is evident from (2.2.22) or (2.2.23) that the distribution $J_c(y,z)$ cannot be derived from the measured $I_s^m(\Phi)$ dependence by performing an inverse Fourier transformation. The reason for that is that in a measurement only the amplitude of the complex function $I_s(\Phi)$ is measured but not the phase. Therefore, the back transformation of $I_s^m(\Phi)$ to obtain $i_c(y,z)$ is not possible.[3]

By making some assumptions about the properties of the function $i_c(z)$ one can restore $i_c(z)$ approximately from the measured $I_s^m(\Phi)$ dependence. For example, if $i_c(z)$ is symmetrical with respect to the junction midpoint, we obtain

$$i_c(z - L/2) = \frac{1}{\pi} \int_0^\infty |I_s^m(k)| \cos(kz)(-1)^{n(k)} dk\ , \tag{2.2.29}$$

where $k = \frac{2\pi}{\Phi_0} t_B B_y$ and n is the number of zeros of $|I_s^m(k)|$ between 0 and k. Analyzing this equation we see that the secondary maxima of the diffraction pattern are increased or reduced, if $i_c(z)$ increases or

[3] We note that in principle also the phase can be measured directly using specific junction configurations. However, this has not yet been used in experiments. See e.g. L. D. Jackel, R. A. Buhrman, W. W. Webb, Phys. Rev. **B 10**, 2782 (1974); J. R. Waldram, J. M. Lumley, Rev. Phys. Appl. **10**, 7 (1975); J. E. Meservey, P. W. Tedrow, D. Paraskevopoulos, IEEE Trans. Magn. **11**, 720 (1975); R. Rifkin, B.S. Deaver, Phys, Rev. **B 13**, 3894 (1976).

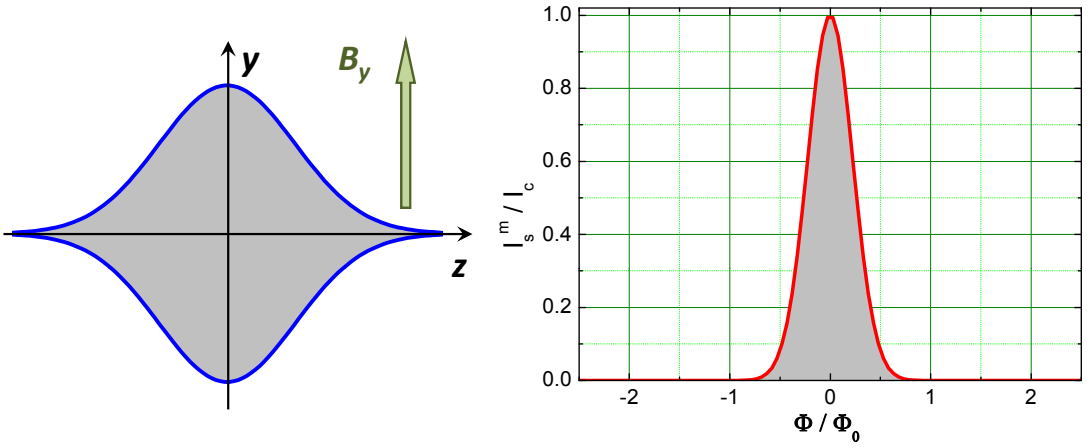

Figure 2.9: Left: Gaussian shaped junction area extending in the yz-plane. For spatially homogeneous $J_c(y,z)$ the current density integrated in y-direction, $i_c(z) = \int J_c(y,z)dy$ corresponds to a Gaussian profile. Right: Magnetic field dependence of the maximum Josephson current as a function of the flux through junction. The magnetic field is applied in y-direction.

decreases towards the junction edges, respectively.[4] Note that $i_c(z)$ is determined by applying the field in y-direction and measuring $I_s^m(\Phi)$. In the same way, we can determine $i_c(y)$ by applying the magnetic field in z-direction and measuring the corresponding $I_s^m(\Phi)$. The two-dimensional distribution $J_c(y,z)$ can be determined by measuring $I_s^m(\Phi)$ for various field directions.

In order to get information on $J_c(y,z)$ on a very small length scale, we have to measure the $I_s^m(\Phi)$ dependence up to high magnetic fields. If we could do a Fourier back transformation, the spatial resolution would be given by $2\pi/k$. With $k = \frac{2\pi}{\Phi_0} t_B B_y$ and $\Phi = B_y t_B L$ we obtain

$$\frac{2\pi}{k} \;=\; \frac{\Phi_0}{t_B}\,\frac{1}{B_y} \;=\; L\,\frac{\Phi_0}{\Phi} \quad . \tag{2.2.30}$$

We see that the spatial resolution is proportional to $1/B_y$. If we are measuring the $I_s^m(\Phi)$ dependence only up to $\Phi/\Phi_0 = 1$, we obtain a spatial resolution only of the order of the junction length L.

In some applications of Josephson junction (e.g. x-ray detectors) the Josephson current has to be suppressed by an applied magnetic field. Therefore, a $I_s^m(\Phi)$ dependence having only a central maximum and vanishing side lobes is desirable. This can be achieved by generating a $i_c(z)$ dependence that is close to a Gaussian profile

$$i_c(z) \;=\; i_c(0)\,\exp\left(-\frac{z^2}{2\sigma^2}\right) \quad . \tag{2.2.31}$$

Since the Fourier transform of a Gaussian profile again is a Gaussian profile, we obtain a $I_s^m(\Phi)$ dependence that has no side lobes

$$I_s^m(\Phi) \;=\; \sqrt{\frac{1}{2\pi}}\, i_c(0) L\,\exp\left(-\sigma k^2\right) \;=\; \sqrt{\frac{1}{2\pi}}\, i_c(0) L\,\exp\left(-\sigma \frac{4\pi^2}{L^2}\frac{\Phi^2}{\Phi_0^2}\right) \quad . \tag{2.2.32}$$

As shown in Fig. 2.9, a Gaussian profile of $i_c(z)$ can be achieved by not choosing a rectangular shaped junction geometry but a shape that well approaches a Gauss curve. For homogeneous $J_c(y,z)$ then $i_c(z)$ is close to a Gauss profile resulting in a good suppression of the side lobes of the $I_c^m(\Phi)$ curve.

[4] A. Barone, G. Paterno, M. Russo, R. Vaglio, physica status solidi **A 41**, 393 (1977).

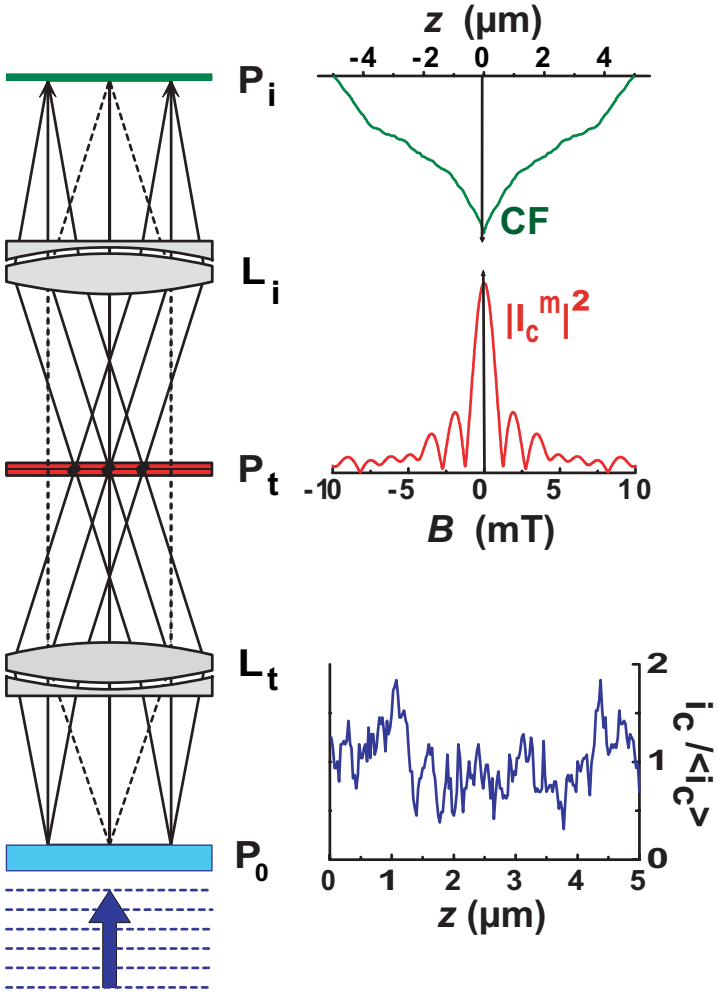

Figure 2.10: Comparison of the measurement of the maximum Josephson current (right) and an optical diffraction experiment (left). Note that in optics the second Fourier transformation recovers an image P_i of the transmission function P_0.

Additional Topic:
The Supercurrent Auto-correlation Function

We briefly compare the measurement of the maximum Josephson current as a function of an applied magnetic field to an optical diffraction experiment (see Fig. 2.10). In the optical diffraction experiment a plane wave is illuminating an object (e.g. a slide) with a transmission function $P_0(z)$. This transmission function corresponds to the spatial distribution $i_c(z)$ of the maximum Josephson current density integrated along the field direction (y-direction for the situation shown in Fig. 2.10). In the simplest case the transmission function is that of an ideal slit, which is constant inside and zero outside the slit. This would correspond to an ideal rectangular shaped junction with spatially homogeneous $J_c(y,z)$. In the more general case the transmission probability or equivalently $i_c(z)$ may vary along z as shown in Fig. 2.10.

For the optics experiment, the measurement of the $I_s^m(B_y)$ dependence corresponds to the observation of the square root of the light intensity P_t in the focal plane after the first lens system L_t. However, in optics in the focal plane both the amplitude and the phase are recovered and, hence, a back-transformation of P_t can be made by a second lens system L_i resulting in an image P_i of the original transmission function P_0. This is just the well known optical imaging process. The spatial resolution of this imaging process

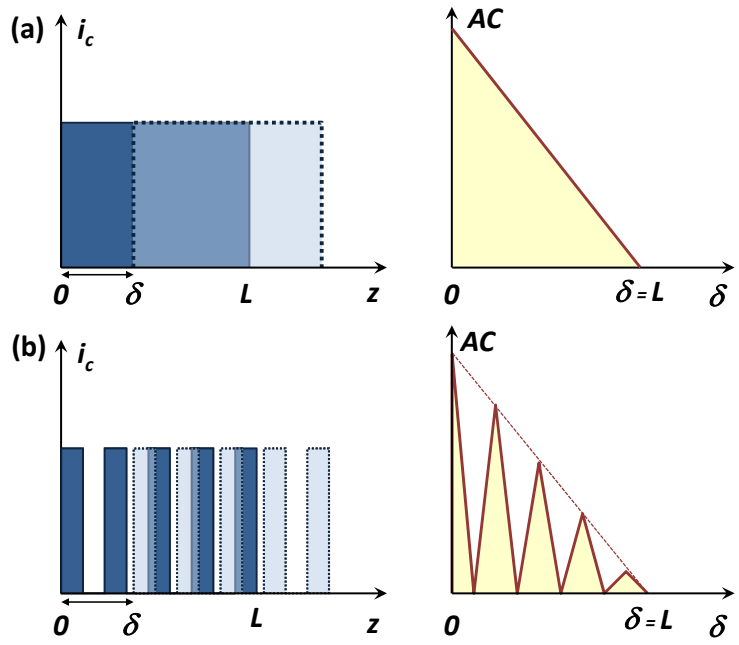

Figure 2.11: (a) The supercurrent auto-correlation function for an ideal slit function $i_c(z)$ obtained for a rectangular shaped Josephson junction with homogeneous critical current density $J_c(y,z)$. (b) The supercurrent auto-correlation function for a periodic function $i_c(z)$. The auto-correlation function shows a modulation with the periodicity of the periodic function.

depends on how many diffraction orders are used for reconstructing the image. In Fig. 2.10 we only have shown the 0^{th} as well as the $\pm 1^{st}$ order for simplicity. For the $I_c^m(B_y)$ measurement, in principle the same process could be performed, if both the amplitude and the phase of $I_c^m(B_y)$ could be measured. Then, in the imaging process the spatial resolution of the $i_c(z)$ image would be given by the number of side lobes of the diffraction pattern used for the reconstruction process. However, as already discussed above, in an experiment we are only measuring the amplitude of $I_c^m(B_y)$ and not the phase. Therefore, in a second Fourier transformation we can back-transform only the intensity $(I_c^m)^2(B_y)$. As we discuss now, the Fourier transform of the intensity distribution is just the auto-correlation function of the supercurrent distribution along the junction.

In general, the auto-correlation function is defined as

$$\mathrm{AC}(\delta) \;=\; \int_{-\infty}^{\infty} i_c(z)\, i_c(z+\delta)\, dz \;. \tag{2.2.33}$$

This expression shows, that the auto-correlation function is just obtained by calculating the overlap between the function $i_c(z)$ and the same function shifted by δ. This is illustrated in Fig. 2.11a, where we have plotted the auto-correlation function for a simple slit function. It is evident that the auto-correlation function is a linearly decreasing function. If the function $i_c(z)$ is not constant across the width L of the slit but varies strongly as schematically shown in Fig. 2.11b, the auto-correlation function no longer shows a linear decrease but a rich fine structure. Only the envelop shows a linear decay.

Using the ***Wiener-Khintchine theorem*** [5,6] we can express the auto-correlation function of the supercur-

[5] N. Wiener, *Generalized harmonic analysis*, Acto Mathematica **55**, 117 (1930).
[6] A. Khintchine, *Korrelationstheorie der stationären stochastischen Prozesse*, Math. Ann. **109**, 604 (1934).

rent distribution $i_c(z)$ in terms of the intensity of the $I_s^m(B_y)$ dependence:

$$\mathrm{AC}(\delta) \;=\; \int_{-\infty}^{\infty} |I_s^m(k)|^2 \; \mathrm{e}^{ik\delta}\, dk \;, \tag{2.2.34}$$

where $k = \frac{2\pi}{\Phi_0} t_B B_y = \frac{1}{L} 2\pi \frac{\Phi}{\Phi_0}$. We immediately see that the spatial information contained in the autocorrelation function depends on the k, or equivalently the magnetic field interval, used in the measurement of the $I_s^m(B_y)$ dependence. According to (2.2.30) we have the spatial resolution $2\pi/k = L\frac{\Phi_0}{\Phi}$. That is, recording the $I_s^m(B_y)$ dependence up to the 100^{th} side lobe (equivalent to $\frac{\Phi_0}{\Phi} = 0.01$) we have a spatial resolution of 0.01 times the junction width.

Note that already the envelop of the $|I_s^m(B_y)|^2$ curve contains valuable statistical information on the supercurrent distribution.[7] If we have for example inhomogeneities of $i_c(z)$, which have a probability distribution $p(a) \propto 1/a$, that is, if the probability times the characteristic length scale a of the inhomogeneity is constant, then the envelop of the $|I_s^m(B_y)|^2$ curve follows a $1/B_y$ dependence. Therefore, we speak about "spatial $1/f$ noise".[8] The presence of such inhomogeneities can be checked easily in the experiment by plotting $\log|I_s^m(B_y)|^2$ versus $\log B_y$. In such a plot one should obtain a straight line with a slope of -1. If, in contrast, the supercurrent distribution would be formed by a random distribution of filaments of width a, then the envelop of the autocorrelation function should be a constant function up to $k = 2\pi/a$ and then should fall off proportional to $1/B_y^2$. In this case we speak of "spatial shot noise".[9] These two examples show that the analysis of the autocorrelation function can yield valuable statistical information on inhomogeneities of the critical current density.

An experimental example is shown in Fig. 2.12. Here, the $I_s^m(B_y)$ dependence of a $YBa_2Cu_3O_{7-\delta}$ grain boundary Josephson junction has been measured up to an applied magnetic field of 5 Tesla. In a $\log|I_s^m(B_y)|$ versus $\log B_y$ plot one obtains a slope of about -0.65 corresponding to $\log|I_s^m(B_y)|^2 \propto 1/B_y^{1.3}$. From this observation one can conclude that there are spatial inhomogeneities in the supercurrent distribution that have a probability distribution $p(a) \propto 1/a^{1.5}$. That is, inhomogeneities with smaller characteristic length scale a have higher probability.

2.2.4 Additional Topic: Direct Imaging of the Supercurrent Distribution

Since it is difficult to derive the spatial distribution of the maximum Josephson current density from measurements of $I_s^m(\Phi)$, direct imaging methods have been developed.[10] In these imaging methods the Josephson junction is scanned by a focused electron or laser beam and the change $\delta I_s^m(y,z)$ of the maximum Josephson current is measured as a function of the beam position (y,z). As discussed in more detail in Appendix B, the measured change $\delta I_s^m(y,z)$ of the integral junction current in first approximation

[7] see e.g. O. M. Fröhlich, H. Schulze, A. Beck, R. Gerdemann, R. Gross, R. P. Huebener, IEEE Trans. Appl. Supercond. **5**, 2188 (1995); O. M. Fröhlich, H. Schulze, A. Beck, B. Mayer, L. Alff, R. Gross, R. P. Huebener, Appl. Phys. Lett. **66**, 2289 (1995).

[8] In the analysis of fluctuating time signals one is plotting the intensity of the Fourier transform of the time signal (the power spectral density S) versus frequency and often obtains a $1/f$ dependence. This is the signature of so-called $1/f$ noise that is ubiquitous in nature. The power spectral density $S(f)$ corresponds to $|I_c^m(B_y)|^2$.

[9] In the analysis of time signals the random appearance of spikes of constant width δt is known to appear due to the discrete nature of physical quantities (e.g. the electronic charge in charge transport). The resulting noise is called shot noise. This noise is white, that is, frequency independent up to high frequencies $f \propto 1/\delta t$ and then falls of as $1/f^2$.

[10] for a review see R. Gross, D. Kölle, *Low Temperature Scanning Electron Microscopy of Superconducting Thin Films and Josephson Junctions*, Reports on Progress in Physics **57**, 651-741 (1994).

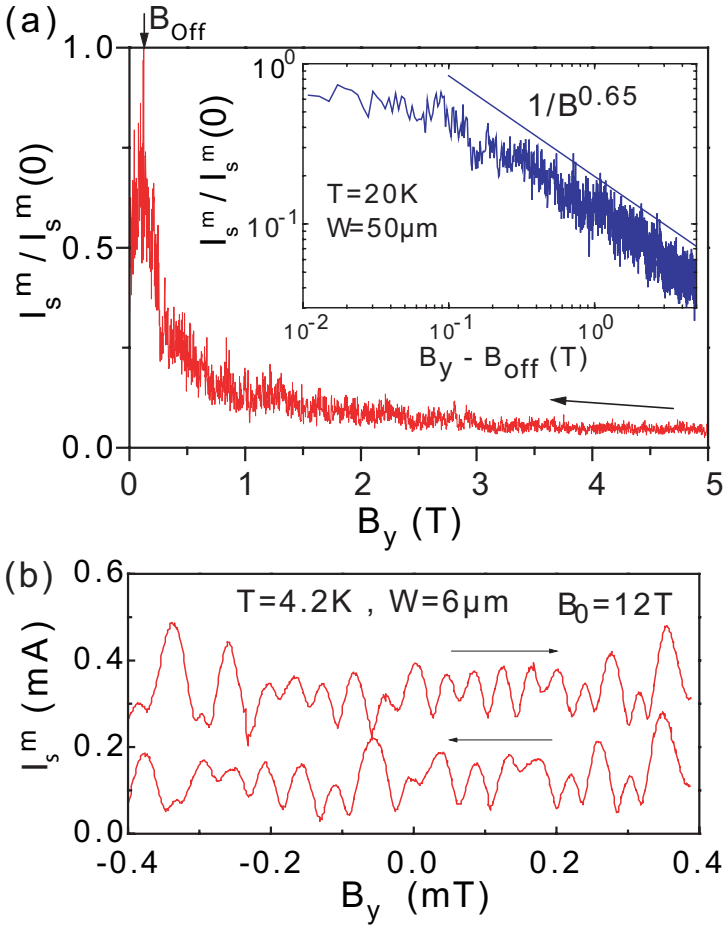

Figure 2.12: (a) I_s^m vs B_y dependence of a $YBa_2Cu_3O_{7-\delta}$ grain boundary Josephson junction recorded for decreasing magnetic field at $T = 20\,\mathrm{K}$. The inset shows I_s^m vs $B_y - B_{\mathrm{off}}$ on a log-log scale. (b) Modulation of I_s^m with varying B_y for opposite sweep directions as indicated by the arrows at a base field $B_0 = 12\,\mathrm{T}$. The curve for increasing field is shifted vertically by $0.2\,\mu\mathrm{A}$ for clarity (from O. Fröhlich ***et al.***, Appl. Phys. Lett. **66**, 2289 (1995)).

is directly proportional to the local critical current density $J_c(y,z)$. Hence, by scanning the junction and measuring $\delta I_s^m(y,z)$ simultaneously, a two-dimensional image of $J_c(y,z)$ is obtained.

The local perturbation of the focused electron or laser beam can be modeled in most cases by a local thermal heating effect. Therefore, the spatial resolution of the imaging technique is not determined by the diameter of the focused electron or laser beam, but by the so-called thermal healing length, which determines the diameter of the heated sample region. Typically, for superconducting thin film structures this length scale is of the order of $1\,\mu\mathrm{m}$.

2.2.5 Additional Topic: Short Josephson Junctions: Energy Considerations

After having found the spatial distribution of the maximum Josephson current density we now discuss the energy E associated with a short Josephson junction. Doing so, we derive a criterion for the notation "short". We will see that short means smaller than a characteristic length scale λ_J, the ***Josephson penetration depth***.

The junction energy is given by the sum

$$E = E_S + E_I \ , \tag{2.2.35}$$

where E_S is the energy stored in the superconducting electrodes and E_I the energy stored in the insulating barrier. The energy stored in the superconducting electrodes is the sum of the magnetic field energy and the kinetic energy of the superelectrons. It is given by

$$E_s = \frac{1}{2\mu_0} \int\limits_{V_s} \left(\mathbf{B}^2 + \mu_0 \Lambda \mathbf{J}_s^2 \right) \, dV \ , \tag{2.2.36}$$

where the integration is over the superconducting volume V_s. This expression, which can be derived from the first London equation, is not valid for the insulating barrier. Here, instead of the kinetic energy of the superelectrons we have to use the Josephson coupling energy E_J. We obtain

$$E_I = \frac{1}{2\mu_0} \int\limits_{V_i} \mathbf{B}^2 \, dV + \int\limits_{V_i} \frac{1}{d} \, \frac{E_J}{A_i} \, dV \ . \tag{2.2.37}$$

Here, $V_i = A_i \cdot d$ is the volume of the insulator with A_i the junction area and d the barrier thickness. With $E_J/A_i = \frac{\Phi_0 J_c}{2\pi}(1-\cos\varphi)$ (compare (2.1.8)) we obtain

$$E_I = \frac{1}{2\mu_0} \int\limits_{V_i} \mathbf{B}^2 \, dV + \int\limits_{A_i} \frac{\Phi_0 J_c(y,z)}{2\pi} \left[1 - \cos\varphi(z) \right] dydz \ . \tag{2.2.38}$$

Here, the second term has been integrated over the barrier thickness d thus leaving only an integral over the junction area A_i extending in the yz-plane.

With (2.2.36) and (2.2.38) we obtain the total energy

$$E = \frac{1}{2\mu_0} \int\limits_{V_s+V_i} \mathbf{B}^2 \, dV + \frac{1}{2} \int\limits_{V_s} \Lambda \mathbf{J}_s^2 \, dV + \int\limits_{A_i} \frac{\Phi_0 J_c(y,z)}{2\pi} \left[1 - \cos\varphi(z) \right] dydz \ . \tag{2.2.39}$$

We are now able to give a definition of a short junction by comparing the different energy contributions. We will call a junction short, if the energy E_B stored in the junction due to the external field (first and second term on the right hand side) is much larger than the Josephson coupling energy E_J (third term on the right hand side), that is $E_B \gg E_J$.

We first consider E_B given by the first two integrals in (2.2.39). If the thickness of the superconducting electrodes is larger than the London penetration depth, the first integral dominates so that

$$E_B = \frac{1}{2\mu_0} \int\limits_{V_s+V_i} \mathbf{B}^2 \, dV \ . \tag{2.2.40}$$

Note that the magnetic flux density penetrates the superconducting electrodes only up to a length given by the London penetration depth. Therefore, the integration volume is given by $W \cdot L \cdot (d + 2\lambda_L) = A_i \cdot t_B$ (compare Fig. 2.4). Hence, we obtain

$$E_B = \frac{1}{2\mu_0} B_y^2 W L t_B = \frac{1}{2\mu_0} \, \frac{\Phi^2 W}{t_B L} \ , \tag{2.2.41}$$

where we have used $\Phi = B_y L t_B$.

We next consider the Josephson coupling energy (energy due to the currents in the junction) given by the last integral in (2.2.39). If we assume for simplicity a spatially homogeneous $J_c(y,z)$, we obtain

$$\begin{aligned} E_J &= \frac{\Phi_0 I_c}{2\pi} - \int_{-W/2}^{W/2}\int_{-L/2}^{L/2} \frac{\Phi_0 J_c(y,z)}{2\pi} \cos\varphi(z)\, dydz \\ &= \frac{\Phi_0 I_c}{2\pi} - \int_{-L/2}^{L/2} \frac{\Phi_0 i_c(z)}{2\pi} \cos\varphi(z)\, dz = \frac{\Phi_0 I_c}{2\pi} - \frac{\Phi_0 I_c}{2\pi} \frac{\sin\frac{\pi\Phi}{\Phi_0}}{\frac{\pi\Phi}{\Phi_0}} \cos\varphi(0) \ , \end{aligned} \tag{2.2.42}$$

where we have used $\varphi(z) = \frac{2\pi\Phi}{\Phi_0}\,\frac{z}{L} + \varphi_0$ (compare (2.2.24)).

Comparing E_J and E_B for the typical flux of one flux quantum in the junction area, the condition $E_B \gg E_J$ can be written as

$$\frac{1}{2\mu_0}\,\frac{\Phi_0^2 W}{t_B L} \gg \frac{\Phi_0 I_c}{2\pi} \ . \tag{2.2.43}$$

With the critical current density $J_c = I_c/WL$ this inequality can be expressed as

$$L \ll \widetilde{\lambda}_J \equiv \sqrt{\frac{\pi\Phi_0}{\mu_0 J_c t_B}} \ . \tag{2.2.44}$$

Hence, a junction is considered short, if its length L is small compared to the characteristic length scale $\widetilde{\lambda}_J$. This length is equal to the so-called ***Josephson penetration depth*** λ_J introduced in section 2.3 within a factor of the order of unity. In the discussion of long Josephson junctions in section 2.3 we will see, how λ_J is entering the equations describing these junction as a natural length scale.

2.2.6 The Motion of Josephson Vortices

Above we have seen that vortices can be used to visualize the Josephson current density in a current driven junction. We now discuss the situation, where Josephson vortices are moving along the junction in z-direction at a constant velocity v_z.

For a short Josephson junction the magnetic field due to the Josephson current density itself can be neglected compared to the external field and we can therefore assume that the flux density in the junction is given by the external field $\mathbf{B}_e = (0, B_y, 0)$. Hence, the gauge-invariant phase difference must satisfy equation (2.2.14):

$$\frac{\partial\varphi}{\partial z} = \frac{2\pi}{\Phi_0} B_y t_B \ . \tag{2.2.45}$$

Due to the motion of the vortices a temporal change of the phase difference at a specific position is obtained. Since the passage of a complete vortex with flux content Φ_0 changes the phase difference by 2π we can write

$$\frac{\partial\varphi}{\partial t} = \frac{2\pi}{\Phi_0}\,\frac{\partial\Phi}{\partial t} \ . \tag{2.2.46}$$

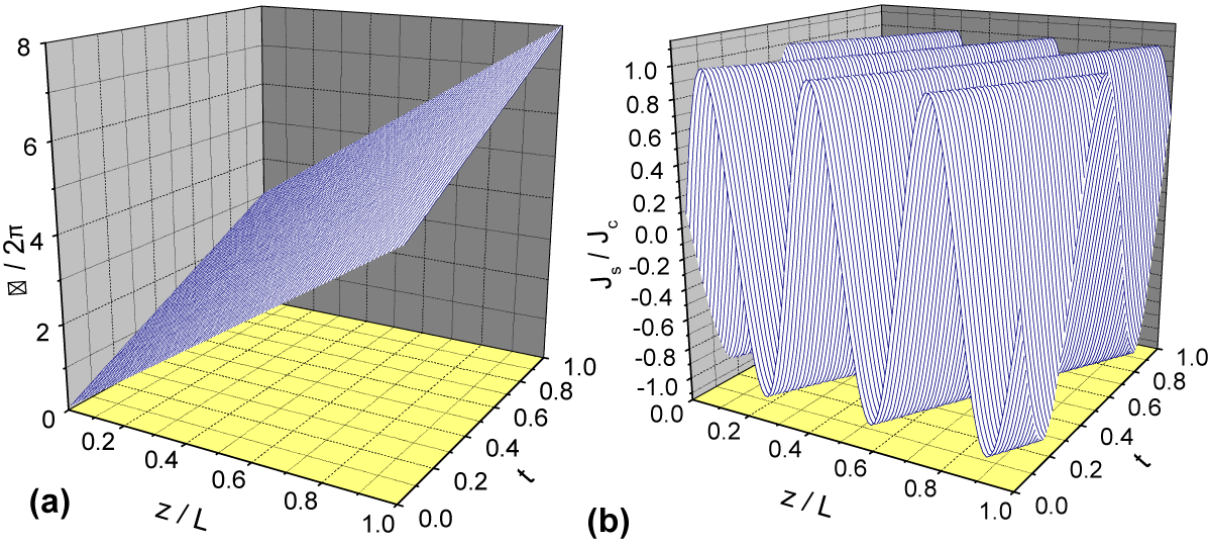

Figure 2.13: (a) The linear increase of the gauge-invariant phase difference along the junction and with increasing time. (b) The corresponding Josephson current density J_s along the junction as a function of time.

With the magnetic flux given by $\Phi = B_y t_B z$ we obtain

$$\frac{\partial \varphi}{\partial t} \;=\; \frac{2\pi}{\Phi_0}\, B_y t_B \frac{\partial z}{\partial t} \;=\; \frac{2\pi}{\Phi_0}\, B_y t_B\, v_z \;. \tag{2.2.47}$$

The solution to (2.2.45) and (2.2.47) is

$$\varphi(z,t) \;=\; \frac{2\pi}{\Phi_0}\, B_y t_B (z - v_z t) + \varphi(0) \;=\; k(z - v_z t) + \varphi(0) \;. \tag{2.2.48}$$

That is, the gauge-invariant phase difference is increasing linearly in space and time. This situation is shown in Fig. 2.13a, where we have plotted $\varphi(z,t)$. In order to obtain the temporal and spatial evolution of the Josephson current density, we have to use the current-phase relation and obtain

$$J_s(y,z,t) \;=\; J_c(y,z)\, \sin\left[k(z - v_z t)\right] \;. \tag{2.2.49}$$

Comparing (2.2.49) to (2.2.17) shows that the current density through the junction has the same spatial pattern as for the stationary vortices but the pattern itself moves at a constant velocity v_z according to our assumption (see Fig. 2.13b).

The current density pattern can be considered as a vortex with a period $p = L\frac{\Phi_0}{\Phi}$. That is, if the flux in the junction corresponds to one flux quantum, $\Phi = \Phi_0$, the period is L. For $\Phi > \Phi_0$ and $\Phi < \Phi_0$ the period is smaller and larger than the junction length L, respectively. With the period p we can define the number of vortices in the junction as

$$N_V \;=\; \frac{L}{p} = \frac{\Phi}{\Phi_0} \;. \tag{2.2.50}$$

The amount $\Delta\varphi$ the gauge-invariant phase difference changes along the junction is then given by

$$\Delta\varphi \;=\; 2\pi\, \frac{\Phi}{\Phi_0} \;=\; 2\pi\, N_V \;. \tag{2.2.51}$$

That is, the change of φ is just given by 2π times the number of vortices in the junction. We can now consider the rate, at which vortices are passing the junction. This rate is given by

$$\frac{dN_V}{dt} = \frac{1}{2\pi}\frac{d\Delta\varphi}{dt} \ . \tag{2.2.52}$$

Since according to the voltage-phase relation a temporal change of the gauge-invariant phase difference is equal to $\frac{2\pi}{\Phi_0}V$, where V is the junction voltage, we obtain

$$\frac{dN_V}{dt} = \frac{V}{\Phi_0} \ . \tag{2.2.53}$$

That is, the constant motion of the vortices across the junction is causing a constant junction voltage proportional to the rate, at which vortices are moving across the junction. We note that this relationship is completely analogous to the motion of Abrikosov vortices across a type-II superconductor perpendicular to the current direction resulting in the so-called flux-flow voltage. A more detailed discussion is given in chapter 3.

2.3 Long Josephson Junctions

In section 2.2 we have neglected the self-field effect by the Josephson current density. This is possible only if the spatial dimensions W, L of the junction are small compared to the Josephson penetration depth. In this section we relax this assumption and discuss long Josephson junctions with spatial dimensions larger than the Josephson penetration depth.

2.3.1 The Stationary Sine-Gordon Equation

We again consider the junction geometry shown in Fig. 2.4. We also note that the derivation of expression (2.2.15) describing the spatial variation of the gauge-invariant phase difference due to a magnetic flux density is general. That is, for the geometry shown in Fig. 2.4 with the external magnetic field applied parallel to the y-direction we can write

$$\frac{\partial \varphi}{\partial z} = \frac{2\pi}{\Phi_0} B_y t_B \ . \tag{2.3.1}$$

However, in contrast to short junctions now the magnetic flux density results both from the externally applied field ***and*** the Josephson current density and must satisfy Ampère's law. With $\mathbf{B} = \mu_0 \mathbf{H}$ and $\mathbf{D} = \varepsilon_0 \mathbf{E}$ we obtain

$$\boldsymbol{\nabla} \times \mathbf{B} = \mu_0 \mathbf{J} + \varepsilon \varepsilon_0 \mu_0 \frac{\partial \mathbf{E}}{\partial t} \ . \tag{2.3.2}$$

Here, μ_0 and ε_0 are the permeability and permittivity in vacuum, respectively, and ε is the dielectric constant of the barrier material.

As in section 2.2 we only consider the zero voltage state, that is, we have $\partial \mathbf{E}/\partial t = 0$. Then, for the geometry of Fig. 2.4 Ampère's law gives

$$\frac{\partial B_y(z)}{\partial z} = -\mu_0 J_x(z) \ . \tag{2.3.3}$$

With this expression we can write the spatial derivative of (2.3.1) as

$$\frac{\partial^2 \varphi(z)}{\partial z^2} = \frac{2\pi\, t_B}{\Phi_0} \frac{\partial B_y(z)}{\partial z} = -\frac{2\pi \mu_0\, t_B}{\Phi_0} J_x(z) \ . \tag{2.3.4}$$

Assuming that $J_c(y,z) = const$ and remembering that the current is flowing in negative x-direction, that is, $J_x(y,z) = -J_s(y,z)$ so that $J_x(z) = -J_c \sin\varphi(z)$ expression (2.3.4) can be rewritten as

$$\boxed{\frac{\partial^2 \varphi(z)}{\partial z^2} = \frac{2\pi \mu_0\, t_B J_c}{\Phi_0} \sin\varphi(z) = \frac{1}{\lambda_J^2} \sin\varphi(z)} \tag{2.3.5}$$

with the ***Josephson penetration depth***

$$\boxed{\lambda_J \equiv \sqrt{\frac{\Phi_0}{2\pi \mu_0 t_B J_c}} \ .} \tag{2.3.6}$$

Note that λ_J is about equal to the characteristic length scale $\widetilde{\lambda}_J$ derived in section 2.2 (compare (2.2.44)) within a factor of the order unity. Equation (2.3.5) shows that the gauge-invariant phase difference follows a nonlinear differential equation called ***stationary Sine-Gordon equation*** (SSGE).[11] Formally, solutions of this equation can be expressed in terms of elliptic Jacobi functions.[12,13] A typical boundary problem for this equation admits, however, several such solutions and only some of them can be realized. In many situations, the stationary Sine-Gordon equation has to be solved numerically.

We close this subsection by emphasizing that for a two-dimensional junction we have the two-dimensional ***stationary Sine-Gordon equation***

$$\frac{\partial^2\varphi(y,z)}{\partial y^2}+\frac{\partial^2\varphi(y,z)}{\partial z^2} \;=\; \frac{1}{\lambda_J^2}\,\sin\varphi(y,z)\;. \tag{2.3.7}$$

Additional Topic:
Analytical Solutions of the SSGE

We consider a few simple cases where we can solve the SSGE (2.3.5) analytically. First we note that we can linearize (2.3.5) for small arguments. Then, with $\sin\varphi\simeq\varphi$ we have

$$\frac{\partial^2\varphi(z)}{\partial z^2} \;=\; \frac{1}{\lambda_J^2}\,\varphi(z) \tag{2.3.8}$$

with the solution

$$\varphi(z) \;=\; \varphi(0)\,\mathrm{e}^{-z/\lambda_J}\;. \tag{2.3.9}$$

Then, from (2.3.1) we obtain for the magnetic field $B_y(z)$ along the junction to

$$B_y(z) \;=\; -\frac{\varphi(0)}{2\pi}\,\frac{\Phi_0}{\lambda_J t_B}\,\mathrm{e}^{-z/\lambda_J}\;. \tag{2.3.10}$$

This expression shows that λ_J is a decay length for the magnetic field justifying the expression penetration depth.

With $\frac{\partial B_y(z)}{\partial z}=-\mu_0 J_x(z)$, for the current flowing at the edges of the junction we obtain

$$J_x(z=0) \;=\; \frac{1}{\lambda_J}\,\frac{B_y(z=0)}{\mu_0}\;. \tag{2.3.11}$$

Since the junction can stay in the Meißner state as long as $J_x\le J_c$, Meißner solutions are possible for

$$B_y(z=0) \;\le\; \mu_0 J_c\lambda_J\;. \tag{2.3.12}$$

We next consider the case of a small junction with $L\ll\lambda_J$. Equation (2.3.5) can then be approximated by $\frac{\partial^2\varphi(z)}{\partial z^2}\simeq 0$ resulting in $\frac{\partial\varphi(z)}{\partial z}\simeq const$. That is, we obtain the well known result of the short junction. Note that according to (2.3.4) the approximation $\frac{\partial^2\varphi(z)}{\partial z^2}\simeq 0$ is equivalent to neglecting the self-field effect of the current. This again demonstrates that the condition for a short junction is equivalent to the assumption of neglecting self-fields.

[11] J. Rubinstein, J. Math. Phys. **11**, 258 (1970).
[12] I.O. Kulik, Sov. Phys. JETP **51**, 1952 (1966).
[13] C.S. Owen, D.J. Scalapino, Phys. Rev. **164**, 538 (1967).

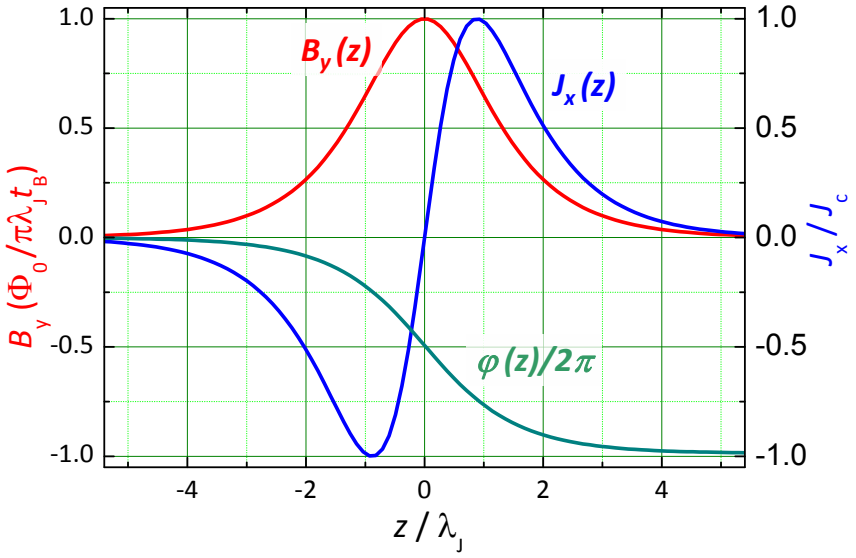

Figure 2.14: Magnetic flux and current density distribution as well as the variation of the gauge-invariant phase difference for a the Josephson vortex solution of the stationary Sine-Gordon equation.

2.3.2 The Josephson Vortex

A possible solution of the SSGE is the particular solution

$$\varphi(z) = \pm 4 \arctan\left\{\exp\left(\frac{z-z_0}{\lambda_J}\right)\right\} + 2\pi n \tag{2.3.13}$$

which can be verified by substitution into (2.3.5). The corresponding magnetic field can be found from (2.3.1) to

$$B_y(z) = \pm\frac{\Phi_0}{\pi\lambda_L t_B}\,\frac{1}{\cosh\left(\frac{z-z_0}{\lambda_J}\right)}\ . \tag{2.3.14}$$

The Josephson current density is obtained form (2.3.3) to

$$J_x(z) = -J_s(z) = = \pm\frac{\Phi_0}{\pi\mu_0\lambda_L^2 t_B}\,\frac{\sinh\left(\frac{z-z_0}{\lambda_J}\right)}{\cosh\left(\frac{z-z_0}{\lambda_J}\right)} \tag{2.3.15}$$

$$= \pm 2J_c\,\frac{\sinh\left(\frac{z-z_0}{\lambda_J}\right)}{\cosh\left(\frac{z-z_0}{\lambda_J}\right)}\ . \tag{2.3.16}$$

Note that for a general solution of a differential equation we not only have to know the particular solution but also the homogeneous solutions in order to match the boundary conditions. However, we will restrict ourselves here to those cases where only the particular solution is needed.

A particular important example is the case where the origin is chosen at z_0 and $\varphi(z)$ is chosen to vanish at $z = \pm\infty$ in a junction of infinite length. In this case the particular solution is the full solution satisfying the boundary conditions. The corresponding magnetic field and current distribution is shown in Fig. 2.14.

The magnetic field and the Josephson current density decay with the characteristic length scale λ_J. Interestingly, the Josephson current density does not have a maximum at the position where the magnetic field has its maximum. Integrating the magnetic flux density and the current density along the junction we see that the total Josephson current is zero and the total flux is equal to Φ_0. That is, we have a situation similar to that shown in Fig. 2.6c and Fig. 2.8. Therefore, we can interpret this special solution of the SSGE as a ***Josephson vortex*** in a long Josephson junction. The different signs in (2.3.13) – (2.3.16) correspond to different orientations or polarizations of the vortex. It is evident that the Josephson vortex is confined to a length of the order of the Josephson penetration depth λ_J.

Additional Topic:
Energy of the Josephson Vortex Solution

As we have done for a short junction, we can calculated the energy E for a long Josephson junction. In fact the expression (compare (2.2.39))

$$E = \frac{1}{2\mu_0}\int\limits_{V_s+V_i} \mathbf{B}^2\, dV + \frac{1}{2}\int\limits_{V_s} \Lambda \mathbf{J}_s^2\, dV + \int\limits_{A_i} \frac{\Phi_0 J_c(y,z)}{2\pi}\,[1-\cos\varphi(z)]\, dydz \tag{2.3.17}$$

also holds for long Josephson junctions with the energy (compare (2.2.36))

$$E_s = \frac{1}{2\mu_0}\int\limits_{V_s} \left(\mathbf{B}^2 + \mu_0 \Lambda \mathbf{J}_s^2\right)\, dV \tag{2.3.18}$$

stored in the superconductor and the energy (compare (2.2.38))

$$E_I = \frac{1}{2\mu_0}\int\limits_{V_i} \mathbf{B}^2\, dV + \int\limits_{A_i} \frac{\Phi_0 J_c(y,z)}{2\pi}\,[1-\cos\varphi(z)]\, dydz\ . \tag{2.3.19}$$

stored in the insulator.

In the following we calculate the stored energy for the vortex solution of the long junction. Here, we again assume that the junction electrodes are much thicker than the London penetration depth so that the first term dominates in the expression for E_s. Then we have

$$E = \frac{1}{2\mu_0}\int\limits_{V_s+V_i} \mathbf{B}^2\, dV + \int\limits_{A_i} \frac{\Phi_0 J_c(y,z)}{2\pi}\,[1-\cos\varphi(z)]\, dydz\ . \tag{2.3.20}$$

Using $\partial\varphi/\partial z = 2\pi B_y t_B/\Phi_0$ to express the magnetic flux density B_y in terms of the gauge-invariant phase difference φ, we obtain after integrating over y and x [14]

$$E = \frac{\Phi_0 J_c W}{2\pi}\int\limits_{-\infty}^{\infty} \left\{ \frac{1}{2}\lambda_J^2 \left(\frac{\partial\varphi(z)}{\partial z}\right)^2 + [1-\cos\varphi(z)] \right\} dz\ . \tag{2.3.21}$$

[14] We obtain $B_y^2/2\mu_0 = (\partial\varphi/\partial z)^2\,\Phi_0^2/8\pi^2 t_B^2\mu_0 = (\partial\varphi/\partial z)^2(\Phi_0 J_c/2\pi t_B)\frac{1}{2}\lambda_J^2$. Integration over y gives just the junction width W and integration over x gives the magnetic thickness t_B. That is $\iint(\Phi_0 J_c/2\pi t_B)\frac{1}{2}\lambda_J^2\, dxdy = (\Phi_0 J_c W/2\pi)\ \frac{1}{2}\lambda_J^2$.

With the expression (2.3.13) for $\varphi(z)$ we can now calculate the energy stored in the vortex solution. In order to do so we use the trigonometric identity $1-\cos\varphi = 2\sin^2(\varphi/2)$. With $\varphi(z) = 4\arctan\left\{\exp\left(\frac{z-z_0}{\lambda_J}\right)\right\} = -2\sin^{-1}(1/\cosh(z/\lambda_J))$ we obtain

$$1-\cos\varphi(z) \;=\; 2\,\frac{1}{\cosh^2\left(\frac{z}{\lambda_J}\right)}\;. \tag{2.3.22}$$

Furthermore, the first term in the integral can be simplified by using (2.3.14):

$$\frac{1}{2}\lambda_J^2\left(\frac{\partial\varphi}{\partial z}\right)^2 \;=\; 2\,\frac{1}{\cosh^2\left(\frac{z}{\lambda_J}\right)}\;. \tag{2.3.23}$$

Hence, we obtain

$$E \;=\; \frac{2\Phi_0 J_c W}{\pi}\int_{-\infty}^{\infty}\frac{1}{\cosh^2\left(\frac{z}{\lambda_J}\right)}\,dz \;=\; \frac{4\Phi_0 J_c W\lambda_J}{\pi}\;. \tag{2.3.24}$$

With this expression we can write down the energy per unit length of the Josephson vortex to

$$\boxed{E_{\text{Vortex}} \;=\; \frac{E_I}{W} \;=\; \frac{4\Phi_0 J_c\lambda_J}{\pi}\;.} \tag{2.3.25}$$

Note that the energy of the vortex is positive. That is, its formation is impossible without external fields and/or currents supplying the required energy.

With expression (2.3.25) for the vortex energy per unit length we can find the magnetic flux density B_{c1}, at which the vortex will first enter the junction in complete analogy to the lower critical field of a type-II superconductor.[15] For a type-II superconductor the lower critical field is given by

$$B_{c1} \;=\; \frac{\mu_0}{\Phi_0}\,E_{\text{Vortex}}\;. \tag{2.3.26}$$

Hence, in analogy the lower critical field of a long Josephson junction is

$$\boxed{B_{c1} \;=\; \frac{4\mu_0 J_c\lambda_J}{\pi} \;=\; \frac{2\Phi_0}{\pi^2\lambda_J t_B}\;.} \tag{2.3.27}$$

This result can be understood intuitively. B_{c1} is just about the magnetic flux density of a single flux quantum distributed over an area $t_B\cdot\lambda_J$.

[15] see e.g. T. P. Orlando, K. A. Delin, *Foundations of Applied Superconductivity*, Addison-Wesley, New York (1991); section 6.5.

2.3.3 Junction Types and Boundary Conditions

If we consider the stationary Sine-Gordon equation (SSGE) we see that only the properties of the tunneling barrier (barrier thickness d or equivalently J_c) and the junction electrodes (London penetration depth λ_L) are entering. In contrast, the geometry of the junction electrodes are not entering the differential equation. However, the geometry of the junction electrodes determine how the current is flowing into the junction area and therefore is entering the boundary conditions.

In order to solve the SSGE we have to know the magnetic flux density at the edges of the junction. That is, we have to know the boundary conditions (compare (2.2.15))

$$\left.\frac{\partial\varphi}{\partial z}\right|_{z=0} = \left.\frac{2\pi t_B}{\Phi_0}B_y\right|_{z=0} \tag{2.3.28}$$

$$\left.\frac{\partial\varphi}{\partial z}\right|_{z=L} = \left.\frac{2\pi t_B}{\Phi_0}B_y\right|_{z=L} \tag{2.3.29}$$

$$\left.\frac{\partial\varphi}{\partial y}\right|_{y=0} = -\left.\frac{2\pi t_B}{\Phi_0}B_z\right|_{y=0} \tag{2.3.30}$$

$$\left.\frac{\partial\varphi}{\partial y}\right|_{y=W} = -\left.\frac{2\pi t_B}{\Phi_0}B_z\right|_{y=W} \quad . \tag{2.3.31}$$

The main problem is that the magnetic flux density is determined by both the external applied flux density $\mathbf{B}^{ex}$ ***and*** the flux density $\mathbf{B}^{el}$ of the current density in the junction electrodes:

$$\mathbf{B} = \mathbf{B}^{ex} + \mathbf{B}^{el} \quad . \tag{2.3.32}$$

In contrast to short junctions we no longer can neglect $\mathbf{B}^{el}$. Unfortunately, in many cases the geometry of the junction electrodes is complicated and, hence, it is difficult to calculate the magnetic flux density at the junction edges. Moreover, the current density distribution in the junction electrodes is determined by the spatial distribution of the Josephson current density itself. That is, the boundary conditions depend on the solution of the SSGE. Therefore, in many cases numerical iteration methods have to be used to solve the SSGE self-consistently.[16,17,18]

In the following we discuss the boundary conditions for a few simple one-dimensional junction geometries. Here, one-dimensional means that the junction dimension in one direction (the y-direction in the following) is much smaller than the Josephson penetration depth. Then, for this junction direction self-field effects of the current can be usually neglected. In the following subsections we classify the junctions into three main types, namely

- ***overlap junctions***,
- ***inline junctions***, and
- ***grain boundary junctions***.

[16] J. Mannhart, J. Bosch, R. Gross, R. P. Huebener, *Calculation of the Josephson Current Distribution in Two-dimensional Tunnel Junctions*, Phys. Lett. **A 121**, 241 (1987).

[17] J. Mannhart, J. Bosch, R. Gross, R. P. Huebener, *Spatial Distribution of the Maximum Josephson Current in Superconducting Tunnel Junctions*, J. Low Temp. Phys. **70**, 459 (1988).

[18] B. Mayer, H. Schulze, G. M. Fischer, R. Gross, *Nonlocal Response of Grain Boundary Type Josephson Junctions to Local Perturbation*, Phys. Rev. **B 52**, 7727 (1995).

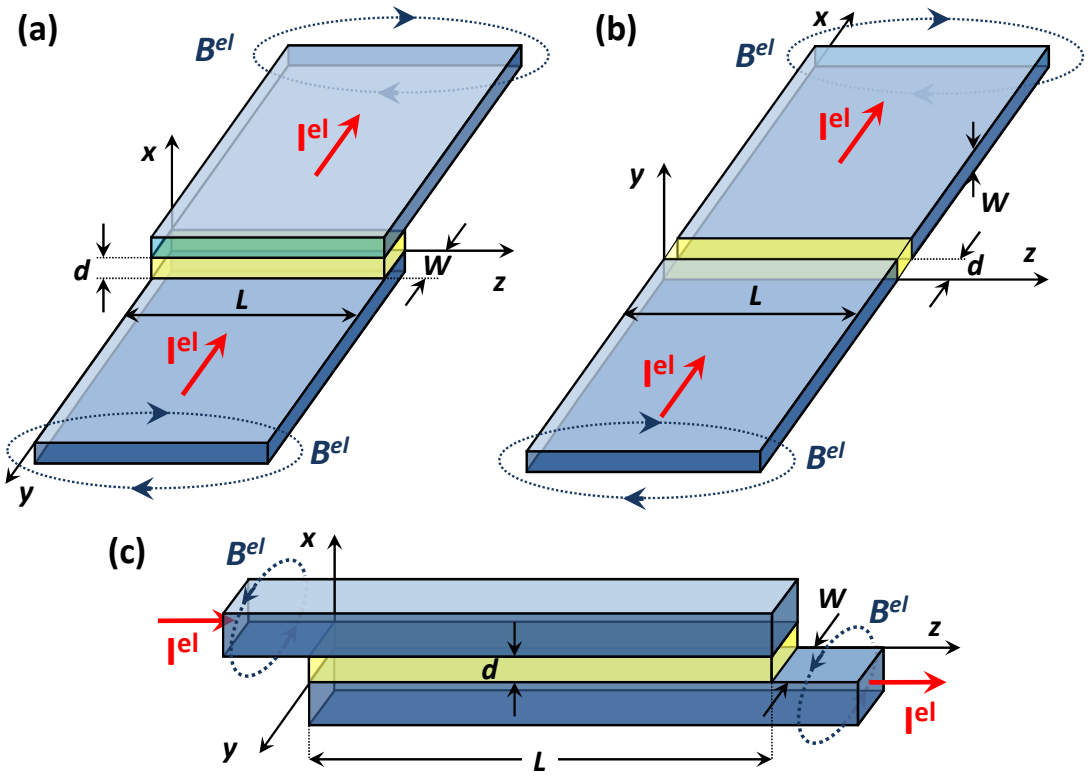

Figure 2.15: The geometry of the overlap (a), the grain boundary (b) and the inline Josephson junction (c). The junction plane always extends in the yz-plane. The width W of the junction is small, whereas the length L of the junction is large compared to the Josephson penetration depth λ_J. Also indicated is the direction of the electrode current I^{el} and the resulting magnetic field B_{el}.

We discuss the boundary conditions for these junction types and the resulting stationary Sine-Gordon equation.

The geometries of the three main junction types are shown in Fig. 2.15. For the ***overlap junction*** the junction area is formed by a short overlap of width W of the bottom and the top junction electrodes extending in y-direction. The one-dimensional junction of length L extends in z-direction, that is, perpendicular to the direction of the current flow in the electrodes (x-direction). Therefore, the magnetic field B^{el} generated by the electrode current I^{el} at the junction edges is parallel to the z-direction and, hence, perpendicular to the short side of the junction. Therefore, the magnetic flux $\Phi^{el} = B^{el} W t_B$ is negligibly small due to the very small width W of the junction. Note that the field component B_x^{el} is perpendicular to the junction area and has no influence on the gauge-invariant phase difference (compare (2.2.15)).

For the ***inline junction*** the situation is different. Here, the junction area is formed by a long overlap of length L of the bottom and the top junction electrodes extending in the z-direction. The width W again is very small so that we have a one-dimensional junction extending in the z-direction. The important point is that in contrast to the overlap junction the long side of the junction now is parallel to the direction of the current flow in the electrodes (z-direction). Therefore, the magnetic field B^{el} generated by the electrode current I^{el} at the junction edges is parallel to the y-direction and, hence, perpendicular to the long side of the junction. Therefore, the magnetic flux $\Phi^{el} = B^{el} L t_B$ is significant due to the large length $L \gg \lambda_J$ of the junction and has to be taken into account. As for the overlap junction the field component B_x^{el} is perpendicular to the junction area and therefore has no influence on the gauge-invariant phase difference.

For the ***grain boundary junction*** geometry we have somehow a mixture of the overlap and inline geometry. Here, the junction area is not formed by an overlap of the bottom and the top electrode, but both

electrodes are attached to each other face to face. This junction configuration has been widely used for the high temperature superconductors. For these materials a Josephson junction could be obtained by putting an epitaxial film on a bicrystalline substrate. Since the high temperature superconducting film takes the in-plane orientation of the bicrystalline substrate, an individual grain boundary could be introduced into the epitaxial film with the grain boundary angle determined by the substrate. This artificial grain boundary was found to act as junction barrier resulting in a Josephson junction.[19] Therefore, this junction type is called grain boundary Josephson junction. In the grain boundary geometry the junction area extending in the yz-plane is not parallel to the surface of the electrodes (xz-plane) as for the overlap and inline geometry but perpendicular to it. Therefore, the electrode current I^{el} is now flowing perpendicular to the junction area and not parallel to it as for the overlap and inline geometry. The width W of the junction is small and the length L of the junction large compared to the Josephson penetration depth resulting in a one-dimensional junction extending in the z-direction. In contrast to the overlap and inline geometry now both the y- and z-component of the magnetic field B^{el} generated by the electrode current I^{el} lie in the junction plane. Whereas the component B_z^{el} can be neglected due to the small width W of the junction, the component B_y^{el} has to be taken into account, since it is perpendicular to the long side of the junction.

Overlap Junctions

For the overlap junction the magnetic field B_z^{el} due to the electrode current flowing in the bottom and top electrode can be expressed as[20]

$$B_z^{el} \simeq \pm\frac{\mu_0}{2}\frac{I^{el}}{L} \ . \tag{2.3.33}$$

We see that the electrode current is generating only a field component in z-direction. With the external magnetic field applied in y-direction, the total field in z-direction is only determined by B^{el} and we can write the boundary conditions (2.3.30) and (2.3.31) as[21]

$$\left.\frac{\partial\varphi}{\partial y}\right|_{y=0} = +\frac{2\pi t_B}{\Phi_0}B_z^{el}\Big|_{y=0} = +\frac{1}{\lambda_J^2}\frac{I^{el}}{2J_cL} \tag{2.3.34}$$

$$\left.\frac{\partial\varphi}{\partial y}\right|_{y=W} = -\frac{2\pi t_B}{\Phi_0}B_z^{el}\Big|_{y=W} = -\frac{1}{\lambda_J^2}\frac{I^{el}}{2J_cL} \ . \tag{2.3.35}$$

With $W \ll \lambda_J$, the gauge-invariant phase difference φ can have only a very small variation in y-direction. Therefore, we can use the Ansatz

$$\varphi(y,z) = \varphi(z) + f(y) \ .$$

With the boundary conditions (2.3.34) and (2.3.35) we obtain for an arbitrary y position between the two edges

$$\frac{\partial f}{\partial y} = \frac{2\pi t_B}{\Phi_0}\frac{\mu_0 I^{el}}{2L}\left(1-\frac{2y}{W}\right)$$

[19] For a review see R. Gross, *Grain Boundary Josephson Junctions in the High Temperature Superconductors* in *Interfaces in High-T_c Superconducting Systems*, S. L. Shinde and D. A. Rudman eds., Springer Verlag, New York (1994), pp. 176-210.

[20] We use $\oint Bds = \mu_0 I^{el}$ and $\oint Bds \simeq B_z^{el}\cdot 2L$. We also assume that the current distribution in the electrodes is homogeneous. The case of an inhomogeneous current distribution will be discussed below in the subsection on mixed overlap and inline junction geometries.

[21] Note that B_z^{el} is in negative z-direction for $y=0$ and in positive z-direction for $y=W$.

and hence

$$\frac{\partial^2\varphi}{\partial y^2} = -\frac{2\pi t_B}{\Phi_0}\frac{\mu_0 I^{el}}{LW} = -\frac{2\pi t_B\mu_0 J_c}{\Phi_0}\frac{I^{el}}{I_c} = -\frac{1}{\lambda_J^2}\frac{I^{el}}{I_c} = -\frac{1}{\lambda_J^2}\gamma\ , \tag{2.3.36}$$

where $\gamma \equiv I^{el}/I_c$. With the solution for $\frac{\partial^2\varphi}{\partial y^2}$ we obtain from (2.3.7)

$$\boxed{\frac{\partial^2\varphi(z)}{\partial z^2} - \frac{1}{\lambda_J^2}\sin\varphi(y,z) = \frac{1}{\lambda_J^2}\gamma\ .} \tag{2.3.37}$$

For the field component in y-direction we have $B_y = B_y^{ex}$ and we obtain the boundary conditions

$$\boxed{\left.\frac{\partial\varphi}{\partial z}\right|_{z=0} = +\frac{2\pi t_B}{\Phi_0}B_y^{ex}\Big|_{z=0}} \tag{2.3.38}$$

$$\boxed{\left.\frac{\partial\varphi}{\partial z}\right|_{z=L} = +\frac{2\pi t_B}{\Phi_0}B_y^{ex}\Big|_{z=L}\ .} \tag{2.3.39}$$

Inline Junctions

For the inline junction the magnetic field B_y^{el} due to the electrode current flowing in the bottom and top electrode can be expressed as

$$B_y^{el} \simeq \pm\frac{\mu_0}{2}\frac{I^{el}}{W}\ . \tag{2.3.40}$$

We see that the electrode current is generating only a field component in y-direction. With the external magnetic field applied in y-direction, the total field in y-direction is then determined by the sum $B_y^{ex} + B_y^{el}$.

Since $W \ll \lambda_J$ and since we have no magnetic field component in z-direction, we can assume $\frac{\partial^2\varphi}{\partial y^2} \simeq 0$ and we arrive at the differential equation for the inline junction

$$\boxed{\frac{\partial^2\varphi(z)}{\partial z^2} - \frac{1}{\lambda_J^2}\sin\varphi(y,z) = 0\ .} \tag{2.3.41}$$

For the field parallel to the y-direction we have $B_y = B_y^{ex} + B_y^{el}$ and we can write the boundary conditions (2.3.28) and (2.3.29) as[22]

$$\boxed{\left.\frac{\partial\varphi}{\partial z}\right|_{z=0} = +\frac{2\pi t_B}{\Phi_0}\left(B_y^{ex} - \frac{\mu_0 I^{el}}{2W}\right)_{z=0}} \tag{2.3.42}$$

$$\boxed{\left.\frac{\partial\varphi}{\partial z}\right|_{z=L} = +\frac{2\pi t_B}{\Phi_0}\left(B_y^{ex} + \frac{\mu_0 I^{el}}{2W}\right)_{z=L}\ .} \tag{2.3.43}$$

These are the boundary conditions for a so-called symmetric inline junction, where the current in the top and bottom electrode are flowing in the same direction. In an ***asymmetric inline junction*** the current in

[22] Note that the field due to the electrode current is in negative y-direction at $z = 0$ and in positive y-direction for $z = L$.

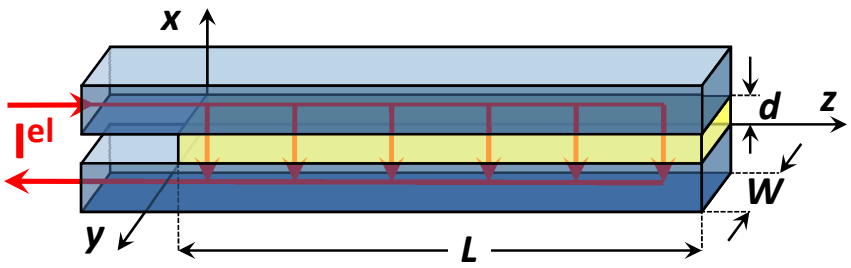

Figure 2.16: The geometry of an asymmetric inline junction. In contrast to the symmetric inline junction the electrode currents in the top and bottom electrode are flowing in opposite direction. At $z = L$ the electrode current density becomes zero, since along the junction length the current injected at $z = 0$ in the top electrode is tunneling to the bottom electrode and flowing back in opposite direction.

the top and bottom electrode are flowing in opposite direction as shown in Fig. 2.16. In this case we have the boundary conditions

$$\left.\frac{\partial\varphi}{\partial z}\right|_{z=0} = +\frac{2\pi t_B}{\Phi_0}\left(B_y^{ex} - \frac{\mu_0 I^{el}}{W}\right)_{z=0} \tag{2.3.44}$$

$$\left.\frac{\partial\varphi}{\partial z}\right|_{z=L} = +\frac{2\pi t_B}{\Phi_0}\left(B_y^{ex}\right)_{z=L} \quad . \tag{2.3.45}$$

These boundary conditions are evident, since now the field at $z = 0$ is twice of that of the symmetric inline junction, whereas the field at $z = L$ vanishes.

Mixed Overlap and Inline Junctions

We can have two situation, where we obtain an inline admixture to an overlap junction geometry:

1. Overlap junctions for which the width of the junction electrodes is larger or smaller than the actual junction length L (see Fig. 2.17a and b).
2. The electrode current is not distributed homogeneously over the cross-section of the electrode. This is the case, if the thickness of the electrodes is larger than the London penetration depth λ_L. Then, the current density distribution in the junction electrodes is peaked at the edges of the junctions (see Fig. 2.17c).

Note that for the overlap geometry the electrode current always was flowing only in y-direction resulting in a magnetic field component B_z^{el} which is perpendicular to the short side of the junction. However, as shown in Fig. 2.17 for the two cases mentioned above there is always a finite electrode current I_z^{el} at the edges of the junction area, which is parallel to the z-direction and results in a magnetic field component B_y^{el} in y-direction. This field component is perpendicular to the long side of the junction and corresponds to the field component of the inline geometry. Therefore, for the situations shown in Fig. 2.17 we speak about a ***mixed overlap and inline geometry***.

The inline admixture to an overlap type junction can be formally characterized by a dimensionless parameter s which ranges between 0 and 1. Here, $s = 0$ corresponds to a pure overlap junction and $s = 1$ to a pure inline junction. With this parameter we obtain the stationary Sine-Gordon equation to

$$\frac{\partial^2\varphi(z)}{\partial z^2} - \frac{1}{\lambda_J^2}\sin\varphi(z) = (1-s)\,\frac{1}{\lambda_J^2}\,\gamma \tag{2.3.46}$$

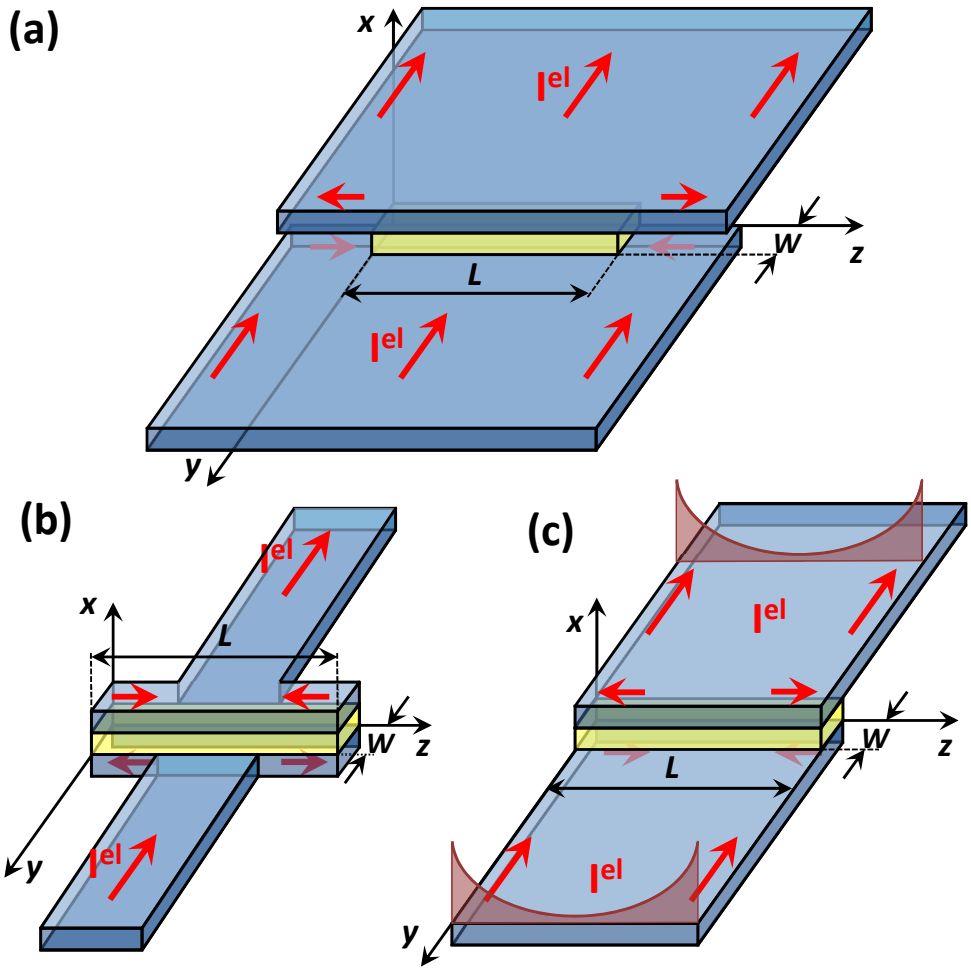

Figure 2.17: The geometry of mixed overlap and inline junctions. In (a) and (b) the width of the electrodes is larger and smaller than the junction length L, respectively, resulting in an electrode current parallel to the z-direction both in the bottom and top electrode. In (c) an electrode current density peaked at the electrode edges results in an electrode current parallel to the z-direction at the edges of the junction area.

with $\gamma \equiv I^{el}/I_c$. The boundary conditions are

$$\left.\frac{\partial\varphi}{\partial z}\right|_{z=0} = +\frac{2\pi t_B}{\Phi_0}\left(B_y^{ex} - s\,\frac{\mu_0 I^{el}}{2W}\right)_{z=0} \tag{2.3.47}$$

$$\left.\frac{\partial\varphi}{\partial z}\right|_{z=L} = +\frac{2\pi t_B}{\Phi_0}\left(B_y^{ex} + s\,\frac{\mu_0 I^{el}}{2W}\right)_{z=L} . \tag{2.3.48}$$

Grain Boundary Josephson Junctions

In grain boundary junctions the junction area is perpendicular to the direction of the electrode currents. This is different to overlap and inline junctions, where the junction area is parallel to the direction of the electrode currents. In contrast to the overlap junction for the grain boundary junction geometry we have to take into account the y-component of the magnetic field B^{el} due to the electrode currents:

$$B_y^{el} \simeq \pm\frac{\mu_0}{2}\,\frac{I^{el}}{L} . \tag{2.3.49}$$

For the overlap geometry this field was perpendicular to the junction area and had no effect on the gauge-invariant phase difference. In contrast, for the grain boundary junctions B_y^{el} is parallel to the junction area. The field component B_y^{el} results in a finite inline admixture. Writing B_y^{el} as

$$B_y^{el} \simeq \pm\frac{\mu_0}{2}\frac{W}{L}\frac{I^{el}}{W} = s\,\frac{\mu_0}{2}\frac{I^{el}}{W} \tag{2.3.50}$$

we see by comparison with (2.3.47) and (2.3.48) that the amount of inline admixture is just $s = W/L \ll 1$, since the length L of the grain boundary junction usually is much larger than the width W. Our analysis shows that the grain boundary junction can be considered as an overlap junction with a small inline admixture. Therefore, we can use the expression for the mixed overlap and inline geometry and the stationary Sine-Gordon equation can be written as

$$\frac{\partial^2\varphi(z)}{\partial z^2} - \frac{1}{\lambda_J^2}\sin\varphi(z) = \left(1-\frac{W}{L}\right)\frac{1}{\lambda_J^2}\gamma = (1-s)\,\frac{1}{\lambda_J^2}\gamma\ . \tag{2.3.51}$$

The boundary conditions are

$$\left.\frac{\partial\varphi}{\partial z}\right|_{z=0} = \frac{2\pi t_B}{\Phi_0}\left(B_y^{ex} + \frac{W}{L}\frac{\mu_0 I^{el}}{2W}\right)_{z=0} \tag{2.3.52}$$

$$\left.\frac{\partial\varphi}{\partial z}\right|_{z=L} = \frac{2\pi t_B}{\Phi_0}\left(B_y^{ex} - \frac{W}{L}\frac{\mu_0 I^{el}}{2W}\right)_{z=L}\ . \tag{2.3.53}$$

We note that for an electrode thickness larger than the London penetration depth λ_L the electrode current is peaked at the junction edges. This results in an additional inline admixture as already discussed above.

2.3.4 Additional Topic: Josephson Current Density Distribution and Maximum Josephson Current

After having found the stationary Sine-Gordon equation and the boundary conditions for the various junction types we can calculate the Josephson current distribution $J_s(y,z)$ in the junction as well as the maximum Josephson current. We perform this calculation only for a few simple cases assuming that the critical current density $J_c(y,z)$ is homogeneous across the junction. We start with the zero field case.

Overlap Junction: $\mathbf{B}^{ex} = 0$

We first consider an overlap junction with a spatially homogeneous electrode current distribution. For zero external magnetic field we have $\partial\varphi/\partial z = 0$ at both junction edges according to (2.3.38) and (2.3.39). Therefore, $\partial^2\varphi/\partial z^2 = 0$ and we obtain the following trivial solution of the SSGE (2.3.36)

$$\varphi(z) = \arcsin(\gamma) + 2\pi n = const. \tag{2.3.54}$$

and hence for the Josephson current density

$$J_s(z) = J_c\,\sin\varphi(z) = const. \tag{2.3.55}$$

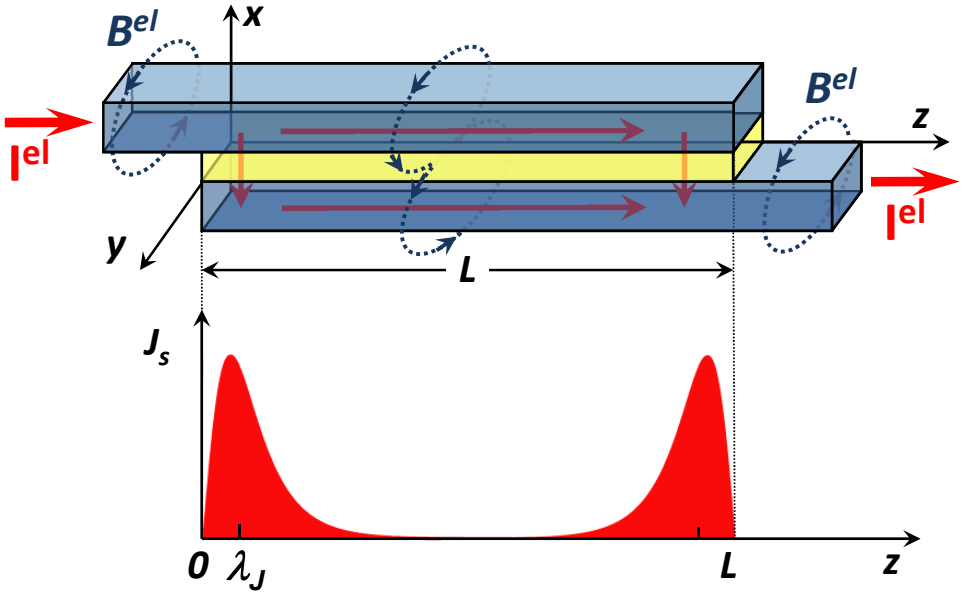

Figure 2.18: The geometry (a) and the Josephson current distribution of a long inline Josephson junction. The Josephson current density J_s is restricted to the boundaries of the junction thereby resulting in the Meißner state of the long inline Josephson junction.

The maximum Josephson current in this case is

$$I_s^m = \int_{A_i} J_s \, dA = J_c \cdot LW = J_c \cdot A_i \ . \tag{2.3.56}$$

Here, $A_i = LW$ is the junction area.

For the overlap junction we obtain the important result that for zero applied magnetic field the Josephson current density is constant across the junction area and the maximum Josephson current is increasing linearly with increasing junction area.

Inline Junction: $\mathbf{B}^{ex} = 0$

In contrast to the overlap junction, for the inline junction we have to take into account the magnetic field due to the electrode current. Qualitatively, we can find the current distribution by recalling that a superconducting system always wants to stay in the Meißner state, that is, it wants to expel the magnetic field. As shown in Fig. 2.18, in an inline junction the Meißner state can be achieved by restricting the Josephson current density to the left and right edge of the junction. Then, the electrode current flowing in the top and bottom electrode are the same along the junction and their magnetic fields cancel each other. In this way the inner of the junction resides in the Meißner state. This situation is similar to a bulk superconductor, where the supercurrent density flows only on the surface of the sample and decays exponentially away from the surface. There, the characteristic decay length is the London penetration depth λ_L. For a Josephson junction an exponential decay is obtained only in the linear approximation (compare (2.3.8) to (2.3.10)). However, due to the nonlinearity of the Sine-Gordon equation the Josephson current density is zero at the edges, increases to the maximum value J_c at a depth equal to about λ_J and than decays again so that the Josephson current density is restricted to an edge region with a length

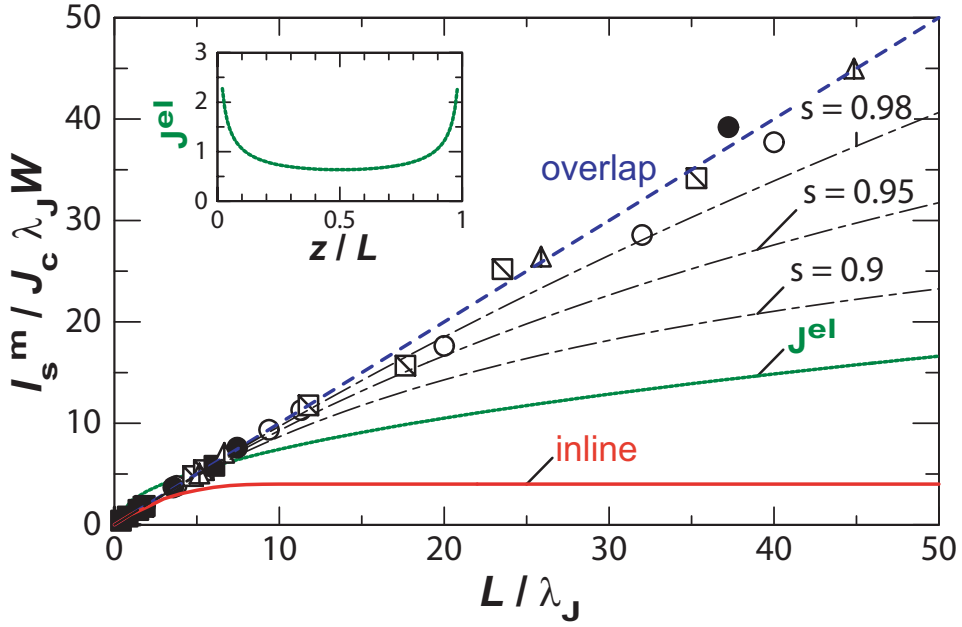

Figure 2.19: The maximum Josephson current I_s^m plotted as a function of the junction length for a pure overlap and inline geometry as well as for different amount s of an inline admixture to the pure overlap geometry. Also shown is the $I_s^m(L)$ dependence for an overlap junction with an inhomogeneous electrode current distribution $J^{el}(z)$ according to (2.3.58).

of about $2\lambda_J$. A detailed calculation shows that the integral maximum Josephson current is

$$I_s^m = \int_{A_i} J_s \, dA = J_c \cdot 4W\lambda_J \ . \tag{2.3.57}$$

That is, in contrast to the overlap junction, for which the maximum Josephson current increases linearly with the junction length, the maximum Josephson current of an inline junction is independent of the junction length L. This is evident from Fig. 2.18. Since the Josephson current density is restricted to the edges of the junction, an increase of the junction length above a value of about $L = 4\lambda_J$ does no longer increase the integral junction current.

Grain Boundary Junction: $\mathbf{B}^{ex} = 0$

For the grain boundary junction we have an overlap type geometry with a certain amount of inline admixture. If the thickness t of the electrodes of the grain boundary Josephson junction is smaller than the London penetration depth, the current distribution in the electrodes is quite homogeneous and, hence, the inline admixture is $s = W/L = t/L$ (compare (2.3.50) and Fig. 2.15). Since usually $t/L \ll 1$, the inline admixture is small and the maximum Josephson current is expected to increase linearly with increasing junction length.

As shown in Fig. 2.19 this has been indeed observed experimentally. The experimental data obtained for the grain boundary junctions follow the theoretical estimate for the overlap junction. Fig. 2.19 also shows that with increasing inline admixture the increase of the maximum Josephson current with increasing junction length L becomes more flat and finally vanishes for a pure inline junction.

In Fig. 2.19 we also show the effect of a spatially inhomogeneous current distribution in the junction electrodes. Assuming for an overlap junction an electrode current distribution

$$J^{el}(z) = \frac{L}{\pi\sqrt{z(L-z)}} , \tag{2.3.58}$$

which is peaked at the edges of the junction, we obtain

$$I_s^m(L) = 2.35\sqrt{L} . \tag{2.3.59}$$

That is, the maximum Josephson current does no longer increase linearly with L but proportional to the square root of the junction length.

The Magnetic Field Dependence of the Maximum Josephson Current

The magnetic field dependence of the maximum Josephson current in the presence of an applied magnetic field has to be calculated numerically in most cases.[23,24,25] A convenient way to calculate the local Josephson current density as well as the integral maximum Josephson current is the use of an iteration method as described in Appendix C.

Fig. 2.20a and b show the magnetic field dependence of the maximum Josephson current for a symmetric overlap junction with a reduced junction length $L/\lambda_J = 5$ and 10. Qualitatively, we can understand the $I_s^m(B^{ex})$ dependence of the symmetric junction as follows: For small applied fields the junction can screen the applied external field by a circulating screening current. This current flows in opposite direction at both junction edges and adds to the external applied transport current. Since the local Josephson current density cannot exceed J_c, the integral maximum Josephson current of the junction decreases, since at one junction edge the screening current flows in the same direction as the transport current. This is shown in Fig. 2.20d where we have plotted the $J_s(z)$ dependence of an overlap junction for increasing applied field. On the left junction edge the screening current is in the same direction as the applied current, whereas it is opposite on the right edge. It can be seen that with increasing applied field the screening current is increasing until it reaches the critical value at the right edge. Then vortices start to penetrate the junction resulting in an oscillating $J_s(z)$ dependence.

We can use Ampère's law $\partial B_y(z)/\partial z = -\mu_0 J_x(z)$ to estimate the maximum field value that can be screened by the junction. Assuming for simplicity an exponential decay of the applied field in the junction, $B_y^{ex}(z) \propto \exp(-z/\lambda_J)$ (linear approximation), we obtain $\partial B_y(z)/\partial z = -\frac{1}{\lambda_J} B_y^{ex}(z) = -\mu_0 J_x(z)$ and hence $J_x = \frac{1}{\lambda_J}\frac{B_y^{ex}}{\mu_0}$. Since $J_x \leq J_c$ we can estimate the maximum field value that can be screened by the junction to $B_c = \mu_0 J_c \lambda_L$. Within a factor of unity this rough estimate is equal to the lower critical field B_{c1} of a long Josephson junction (compare (2.3.27)). Indeed, for $B^{ex} \geq B_{c1} = \frac{4}{\pi}\mu_0 J_c \lambda_J$ a state with one vortex in the junction is energetically more favorable.

The state with no vortex in the junction is called the Meißner state of the junction. For fields larger than the lower critical field B_{c1} a state with one or more vortices inside the junction is more favorable. This can be seen in Fig. 2.20, where the symbols mark the maximum Josephson current values for the different vortex states. It can be seen that for a certain external field the 1-vortex solution has a higher maximum Josephson current than the Meißner state solution, that is, the 1-vortex solution is energetically more

[23] see e.g. A. Barone and G. Paterno, *Physics and Application of the Josephson Effect*, John Wiley & Sons, New York (1982).
[24] S. Pagano, B. Ruggiero and E. Sarnelli, Phys. Rev. **B 43**, 5364 (1991).
[25] S. Pagano, B. Ruggiero, M. Russo and E. Sarnelli, in *Nonlinear Superconductive Electronics and Josephson Devices*, G. Constabile, S. Pagano, N. F. Pedersen, and M. Russo eds., Plenum Press, New York (1991).

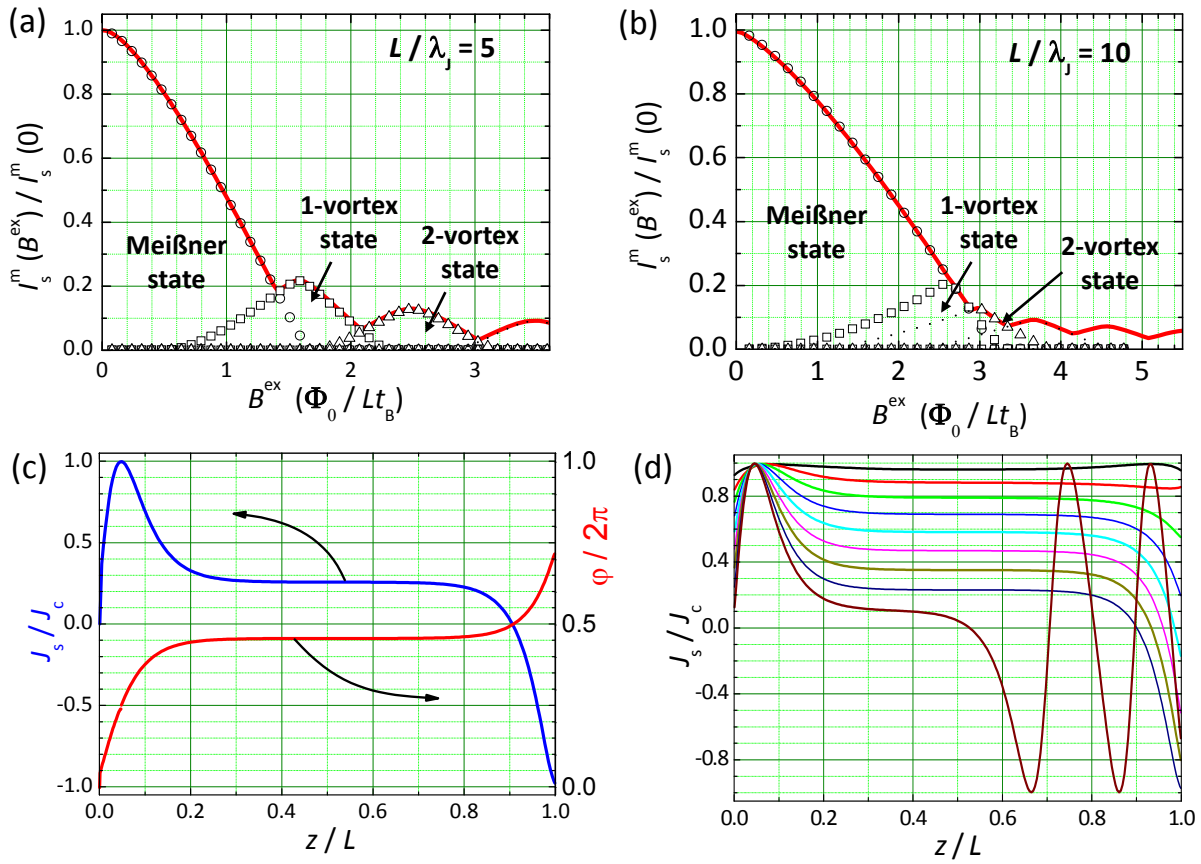

Figure 2.20: I_s^m plotted versus the applied magnetic field B^{ex} for a symmetric overlap junction with $L/\Lambda_J = 5$ (a) und $L/\Lambda_J = 10$ (b). The symbols mark the solutions for the different vortex states. The solid line shows the envelop of the different solutions. In (c) $J_s(z)$ as well as $\varphi(z)$ is shown along the junction for a magnetic field close to B_{c1}. In (d) the change of $J_s(z)$ with increasing applied magnetic field is shown. Only for the highest field vortices can penetrate the junction as can be seen by the oscillating $J_s(z)$ dependence.

favorable. Note that on increasing the magnetic field starting from zero, so that initially the junction is in its Meißner state, the penetration of vortices will start only at a field $B_{\max} > B_{c1}$. This relation can be understood in terms of vortex pinning at the sharp edges of the uniform junction. It can be shown that $B_{\max} = \frac{\pi}{2} B_{c1} = 2\mu_0 J_c \lambda_J$ for an infinitely long junction.[26]

It is also important to note that for a large Josephson junction the variation of the gauge invariant phase difference along the junction is nonlinear (see Fig. 2.20c). This is in contrast to short junctions, where the phase difference was increasing linearly along the junction resulting in a sinusoidal variation of the Josephson current density. The reason for this behavior was the fact that we could neglect the magnetic field of the current and therefore had a spatially homogeneous total magnetic field $B = B^{ex}$. For long junctions, however, we have to take into account the field of the current what results in a spatially varying total field $B = B^{ex} + B^{el}$. Therefore, the spatial variation of $\varphi(z)$ along the junction and, in turn, of the Josephson current density $J_s(z) = J_c \sin\varphi(z)$ is more complicated.

In Fig. 2.21 we have plotted the magnetic field dependence of the maximum Josephson current for symmetric overlap and inline junctions as well as for an asymmetric inline junction. The junctions have a reduced length $L/\lambda_J = 10$. It can be seen that the overlap junction has the highest zero field Josephson current, since here the maximum Josephson current is proportional to the junction length, $I_s^m = J_c W L$. In contrast, as discussed above for the inline junction the maximum Josephson current saturates as a

[26] K. K. Likharev, *Dynamics of Josephson Junctions and Circuits*, Gordon and Breach Science Publishers, New York (1986).

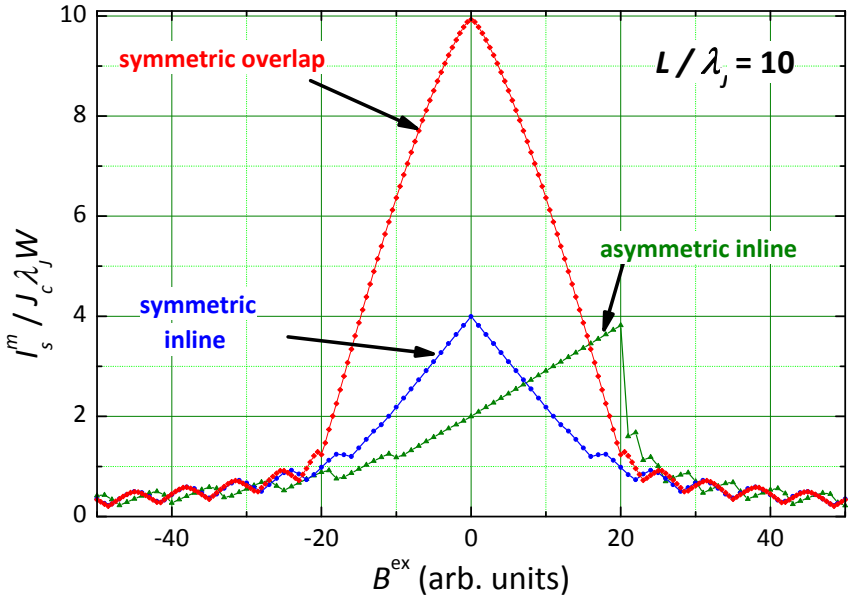

Figure 2.21: I_s^m plotted versus the applied magnetic field B^{ex} for a symmetric overlap and inline junction as well as for an asymmetric inline junction with $L/\Lambda_J = 10$. T

$I_s^m = 4J_c W \lambda_J$. The asymmetric inline junction shows a highly asymmetric $I_s^m(B^{ex})$ dependence. This can be understood as follows (compare Fig. 2.16): The magnetic fields generated by the electrode currents flowing in the bottom and top electrode point in the same direction for the asymmetric inline junction. Now, this field direction can be parallel or anti-parallel to the external field. For anti-parallel orientation the external magnetic field is compensating the field of the electrode currents thereby causing a reduction of the total magnetic field. Therefore the maximum Josephson current is increasing with increasing applied field. In contrast, for parallel orientation the applied field is adding to the field of the electrode currents causing an increase of the total field and, hence, the maximum Josephson current is decreasing with increasing applied field.

2.3.5 The Pendulum Analog

In order to get some insight into the nature of the solutions for φ we recall that the stationary Sine-Gordon equation has the same form as the differential equation for a pendulum. If we make the transcriptions $z \to t$, $\varphi \to \theta$ and $1/\lambda_L^2 \to \omega_0^2 = g/L$, where θ is the angle of the pendulum measured from the top of its circular orbit, and ω_0 is its natural frequency. In terms of this transcription, the solutions for φ found by neglecting the effect of the electrode currents corresponds to the motion of the pendulum whirling around and around with so much kinetic energy that gravitational acceleration is negligible. In the Sine-Gordon equation this limit corresponds to $\lambda_J \to \infty$ so that $d^2\varphi/dz^2 = 0$ and $d\varphi/dz = const$ resulting in a sinusoidal variation of the Josephson current density.

If we consider now a pendulum moving with less energy, but still sufficient energy to have nonzero kinetic energy at the top of the circle, the motion of $\theta(t)$, which is equivalent to $\varphi(z)$, will be periodic but anharmonic. This leads to a non-sinusoidal, periodically reversing current distribution $J_s(z)$. Each cycle of the oscillating current contains one flux quantum. Unlike the sinusoidal case these Josephson vortices are actually localized entities, since they are spaced with a separation exceeding λ_J.

We finally discuss the Meißner limit of a junction of length L. The Meißner solution corresponds to a pendulum moving with an energy that is just sufficient to go over the top. In this case, starting with an

initial angular velocity $(d\theta/dt)_0$ from an initial angle $-\theta_0$ at the time t corresponding to $-L/2$, the pendulum decelerates nearly exponentially as it rises. It moves very slowly for a long time (corresponding to the interior length of the junction), while going over the top, and then exponentially accelerates down the other side, recovering the initial angular velocity at θ_0 (at a time t corresponding to $+L/2$).

If the angular velocity at the top is negligible compared to the initial value, then θ_0 and $(d\theta/dt)_0$ are connected by the conservation of energy and are not independent. Translating back to the junction problem we see that the corresponding initial condition is

$$\left(\frac{2\pi}{\Phi_0}B_y t_B\right)^2 = \left(\frac{d\varphi}{dz}\right)_0^2 = \frac{2}{\lambda_J^2}\left(1-\cos\varphi_0\right) . \tag{2.3.60}$$

Solving this equation for $\cos\varphi_0$, we obtain

$$\cos\varphi_0 = 1-\frac{1}{2}\left(\frac{B_y}{\mu_0 J_c \lambda_J}\right)^2 . \tag{2.3.61}$$

Thus, for small fields we can use the approximation $\cos x = 1-\frac{1}{2}x^2$ and the phase difference φ_0 at the edges of the junction is given by

$$\varphi_0 = \frac{B_y}{\mu_0 J_c \lambda_J} . \tag{2.3.62}$$

If we want to estimate the strongest field that can be screened by the junction, we have to consider the case at which the pendulum is starting from the bottom, that is, $\varphi_0 = \pi$. Then we obtain

$$B_{\max} = 2\mu_0 J_c \lambda_J . \tag{2.3.63}$$

This field is just the highest field for which the Meißner solution is possible. Actually, the screening at $B_{\max}$ is only metastable. The maximum value for which screening is thermodynamically stable has been derived above to $B_{c1} = 4\mu_0 J_c \lambda_J/\pi$ (compare (2.3.27)). Note that for fields close to B_{c1} screening is no longer exponential, but rather becomes so in the interior when φ has become small.

Summary

Short Josephson Junctions:

- We can distinguish between short and long Josephson junctions depending on whether their spatial dimensions (width, length) are smaller or larger than the Josephson penetration depth

$$\lambda_J \equiv \sqrt{\frac{\Phi_0}{2\pi\mu_0 t_B J_c}}$$

- The Josephson coupling energy is given by

$$E_J = \frac{\Phi_0 I_c}{2\pi}(1-\cos\varphi) = E_{J0}(1-\cos\varphi)$$

and can be viewed as a molecular binding energy of two weakly coupled superconductors.

- In an equivalent circuit, an ideal Josephson element can be represented by a nonlinear inductance

$$L_s = \frac{\Phi_0}{2\pi I_c \cos\varphi} = L_c \frac{1}{\cos\varphi} \qquad \text{with} \qquad L_c = \frac{\hbar}{2eI_c} .$$

- The potential energy of a current biased Josephson junction is given by the tilted washboard potential

$$E_{\rm pot}(\varphi) = E_J(\varphi) - \frac{\Phi_0}{2\pi} I = E_{J0}\left[1-\cos\varphi - \frac{I}{I_c}\varphi\right] .$$

- A magnetic field B_y applied parallel to the junction plane (yz-plane) results in a phase gradient

$$\frac{\partial\varphi}{\partial z} = \frac{2\pi}{\Phi_0} B_y t_B$$

in z-direction proportional to B_y and the magnetic thickness t_B. Due to this phase gradient the Josephson current density oscillates in space as

$$J_s(y,z,t) = J_c(y,z)\,\sin\left(\frac{2\pi}{\Phi_0} t_B B_y z + \varphi_0\right) = J_c(y,z)\,\sin(kz+\varphi_0) .$$

The integral Josephson current is given by the modulus of the Fourier transform of $i_c(z)$ (the critical current density integrated along the field direction):

$$I_s^m(B_y) = \left| \int_{-\infty}^{\infty} i_c(z)\, {\rm e}^{\imath kz}\, dz \right|$$

For a rectangular junction with homogeneous critical current density, i_c corresponds to the transmission function of a slit and $I_s^m(B_y)$ is given by a Fraunhofer diffraction pattern.

Long Josephson Junctions:

- The spatial distribution of the gauge invariant phase difference is given by the stationary Sine-Gordon equation (SSGE)

$$\frac{\partial^2\varphi(y,z)}{\partial y^2}+\frac{\partial^2\varphi(y,z)}{\partial z^2} \;=\; \frac{2\pi\mu_0\, t_B J_c}{\Phi_0}\,\sin\varphi(y,z) \;=\; \frac{1}{\lambda_J^2}\,\sin\varphi(y,z)\;.$$

  The solution of the SSGE requires the knowledge of the boundary conditions. Since the boundary conditions are determined by the flux density at the edges of the junction, which in turn depends on $\varphi(y,z)$, a self-consistent solution is required.

- Depending on the boundary conditions, three basic junction types can be distinguished: inline, overlap, and grain boundary junctions.

- A possible solution of the SSGE is the particular solution

$$\varphi(z) \;=\; \pm 4\arctan\left\{\exp\left(\frac{z-z_0}{\lambda_J}\right)\right\}+2\pi n$$

  describing a Josephson vortex.